

Three-dimensional shapelets and an automated classification scheme for dark matter haloes^{*}

C.J. Fluke^{1†}, A.L. Malec¹, P.D. Lasky^{1,2,3}, B.R. Barsdell¹

¹*Centre for Astrophysics & Supercomputing, Swinburne University of Technology, PO Box 218, Hawthorn, Victoria, 3122, Australia*

²*Theoretical Astrophysics, Eberhard Karls University of Tübingen, Tübingen 72076, Germany*

³*School of Physics, University of Melbourne, Parkville, VIC 3010, Australia*

Accepted 18 December 2011

ABSTRACT

We extend the two-dimensional Cartesian shapelet formalism to d -dimensions. Concentrating on the three-dimensional case, we derive shapelet-based equations for the mass, centroid, root-mean-square radius, and components of the quadrupole moment and moment of inertia tensors. Using cosmological N -body simulations as an application domain, we show that three-dimensional shapelets can be used to replicate the complex sub-structure of dark matter halos and demonstrate the basis of an automated classification scheme for halo shapes. We investigate the shapelet decomposition process from an algorithmic viewpoint, and consider opportunities for accelerating the computation of shapelet-based representations using graphics processing units (GPUs).

Key words: methods: data analysis – methods: analytical – (cosmology:) dark matter – (cosmology:) large-scale structure of Universe

1 INTRODUCTION

Complex, three-dimensional structures abound in astronomy on all scales from “fluffy” dust aggregates in molecular clouds (Ossenkopf 1993; Stepnik et al. 2003), to cosmological large-scale structure that has been described as “sponge-like” (Gott, Dickinson & Melott 1986), or a “skeleton” (Sousbie et al. 2008) of clusters, filaments and voids (Barrow, Bhavsar & Sonoda 1985; White et al. 1987).

While aspects of these structures can be expressed in terms of simple, geometrically-motivated properties such as their triaxiality or quadrupole moment, these quantities are not able to capture the higher order complexity of the true shape. The challenge, therefore, is to provide an accurate description of an arbitrary three-dimensional (3-d) shape, possibly over many physical length scales, in the hope that this can lead to improved theoretical or analytical insight into the structure in question.

The human visual system is more than capable of identifying structures and sub-structures for an individual 3-d object, but such qualitative interpretations only have limited use – it is not practical to attempt a classification of shapes by eye when there are many thousands of objects

to inspect.¹ The preferred alternative is an automated approach including:

- decomposition via an appropriate basis set (e.g. Fourier analysis, wavelet transformations);
- partitioning [e.g. Voronoi tessellation - see Icke & van de Weygaert (1987) for an early cosmological application];
- the use of minimal spanning trees to identify connected structures (Barrow et al. 1985; Pearson & Coles 1995);
- Minkowski functionals [which return global geometric properties such as volume, surface area and edge density – Mecke, Buchert & Wagner (1994); Sahni, Sathyaaprakash & Shandarin (1998)]; and
- segmentation [e.g. “dendrograms” used by Goodman et al. (2009) to identify self-gravitating structures in molecular clouds].

The approach we present in this paper is the extension of the two-dimensional (2-d) shapelet method (Refregier 2003) to three dimensions. Shapelets are sets of orthonormal basis functions based on the Hermite polynomial solutions of the quantum harmonic oscillator (QHO). Simple analytic forms can be derived for the physical properties of 3-d structures (e.g. centre of mass, root-mean-square radius and the

^{*} Research undertaken as part of the Commonwealth Cosmology Initiative (CCI: www.thecci.org), an international collaboration supported by the Australian Research Council

[†] cfluke@swin.edu.au

¹ Although, if there are enough individual eyes available to assist, then this approach is feasible, as the Galaxy Zoo project (<http://www.galaxyzoo.org>) has demonstrated.

components of the quadrupole moment and moment of inertia tensors), which can be efficiently calculated in shapelet space.

In astronomy, 2-d shapelets have been applied to image simulation (Massey et al. 2004; Ferry et al. 2008), the morphological classification of galaxies (Kelly & McKay 2004; Andrae, Jahnke & Melchior 2011) and sunspots (Young et al. 2005), and weak gravitational lensing (Refregier & Bacon 2003). The latter includes the measurement of shear (Kuijken 2006), flexion (Goldberg & Bacon 2005), point-spread function modelling and deconvolution (Melchior et al. 2009; Paulin-Henriksson, Refregier & Amara 2009), and weak lensing by large-scale structure from the FIRST radio survey (Chang, Refregier & Helfand 2004). Massey et al. (2007) investigated weak lensing with polar shapelets (Massey & Refregier 2005), a form more suitable for images with rotational symmetry. Further properties of shapelets, including integral relations and convolution sums are presented in Coffey (2006).

The importance of the shapelet approach lies not so much in the basis functions, but in the simplified computation of quantities relating to shape and structure that can be determined once a shapelet decomposition has been obtained. These analytic quantities are expressed as linear sums of weighted shapelet states, greatly reducing the calculation complexity compared to (numerically) solving the related integral formulations.

Shapelet decomposition is not without its problems [see Berry, Hobson & Withington (2004) for an extensive discussion]. Melchior, Meneghetti & Bartelmann (2007) examined the limitations of shapelet image analysis in cases where the orthonormality condition [see equation (6) below] fails, and proposed a decomposition procedure that preserves physical properties of images. Melchior et al. (2010) and Bosch (2010) considered problems with using circular Gaussian basis functions to model galaxies with high ellipticity or a large Sérsic index. Ngan et al. (2009) proposed an alternative orthonormal basis based on the Sérsic profile (hence Sérsiclets) for use in weak lensing analysis. While helping to avoid issues with poor shape recovery from overfitting low signal-to-noise galaxies, and fitting with too many degrees of freedom, Sérsiclets do not possess the analytic properties of shapelets, and the basis functions must be generated numerically. Indeed, it is the existence of analytic functions that has motivated our choice of 3-d Cartesian shapelets as an appropriate tool for quantifying properties of three-dimensional structures.

The remainder of this paper is set out as follows. In Section 2, we present the mathematics of 3- and d -dimensional Cartesian shapelets. New analytic expressions are presented for several important physical properties of 3-d structures in Section 3. In Section 4, we describe issues relating to implementing an efficient 3-d shapelet decomposition code. We highlight the inherent high-degree of parallelism in the shapelet decomposition algorithm, which makes it a promising target for graphics processing units. In Section 5, we present first applications of 3-d shapelets to problems in cosmological simulations, with an emphasis on studying substructure in dark matter halos, demonstrating how an automated shape classifier can work in shapelet space. We end with a summary and outlook for 3-d shapelets in astronomy in Section 6.

2 CARTESIAN SHAPELETS

In this section we present the Cartesian shapelet formalism. For full details of the one- and two-dimensional cases, and applications, see Refregier (2003).

2.1 One-dimensional Cartesian shapelets

The one-dimensional (1-d) shapelet functions are

$$B_n(x; \beta) \equiv \beta^{-1/2} \phi_n(\beta^{-1}x), \quad (1)$$

where β is a scaling length, n is a non-negative integer and

$$\phi_n(x) \equiv \left(2^n \pi^{1/2} n!\right)^{-1/2} H_n(x) e^{-x^2/2} \quad (2)$$

with $H_n(x)$ the n -th order Hermite polynomial. Higher order shapelets can be obtained using the recursion relation (see Appendix A for some useful expressions):

$$B_n(x; \beta) = \left(\frac{x}{\beta}\right) \sqrt{\frac{2}{n}} B_{n-1}(x; \beta) - \sqrt{\frac{n-1}{n}} B_{n-2}(x; \beta) \quad (3)$$

where

$$B_0(x; \beta) = \beta^{-1/2} \pi^{-1/4} e^{-x^2/2\beta^2}, \quad (4)$$

and

$$B_1(x; \beta) = \frac{\sqrt{2}x}{\beta} B_0(x; \beta). \quad (5)$$

The 1-d shapelets form an orthonormal basis, satisfying:

$$\int_{-\infty}^{\infty} B_n(x; \beta) B_m(x; \beta) dx = \delta_{nm} \quad (6)$$

where δ_{nm} is the Kronecker delta symbol. Shapelets are smooth and continuously differentiable everywhere. The shapelet coefficients for a sufficiently well-behaved 1-d function, $f(x)$, are found through the integral:

$$f_n = \int_{-\infty}^{\infty} f(x) B_n(x; \beta) dx \quad (7)$$

allowing the function to be re-written as a sum of (weighted) shapelets:

$$f(x) = \sum_{n=0}^{\infty} f_n B_n(x; \beta). \quad (8)$$

As we show in Section 4, the calculation of f_n poses the main computational challenge. In practice, n is limited to $n \leq n_{\max}$ and the integral of equation (7) is calculated over a finite volume. However, the orthonormality condition assumes infinite support - so power from higher order shapelets may be lost, and the orthonormality requirement may no longer strictly hold if the integration region is too small (Melchior et al. 2007).

2.2 Three-dimensional Cartesian shapelets

Using the orthonormality of 1-d shapelet functions, the basis functions for 2-d shapelets are (Refregier 2003):

$$B_{2,n}(\mathbf{x}; \beta) \equiv \beta^{-1} \phi_{2,n}(\beta^{-1}\mathbf{x}). \quad (9)$$

where

$$\phi_{2,n}(\mathbf{x}) \equiv \phi_{n_1}(x_1) \phi_{n_2}(x_2) \quad (10)$$

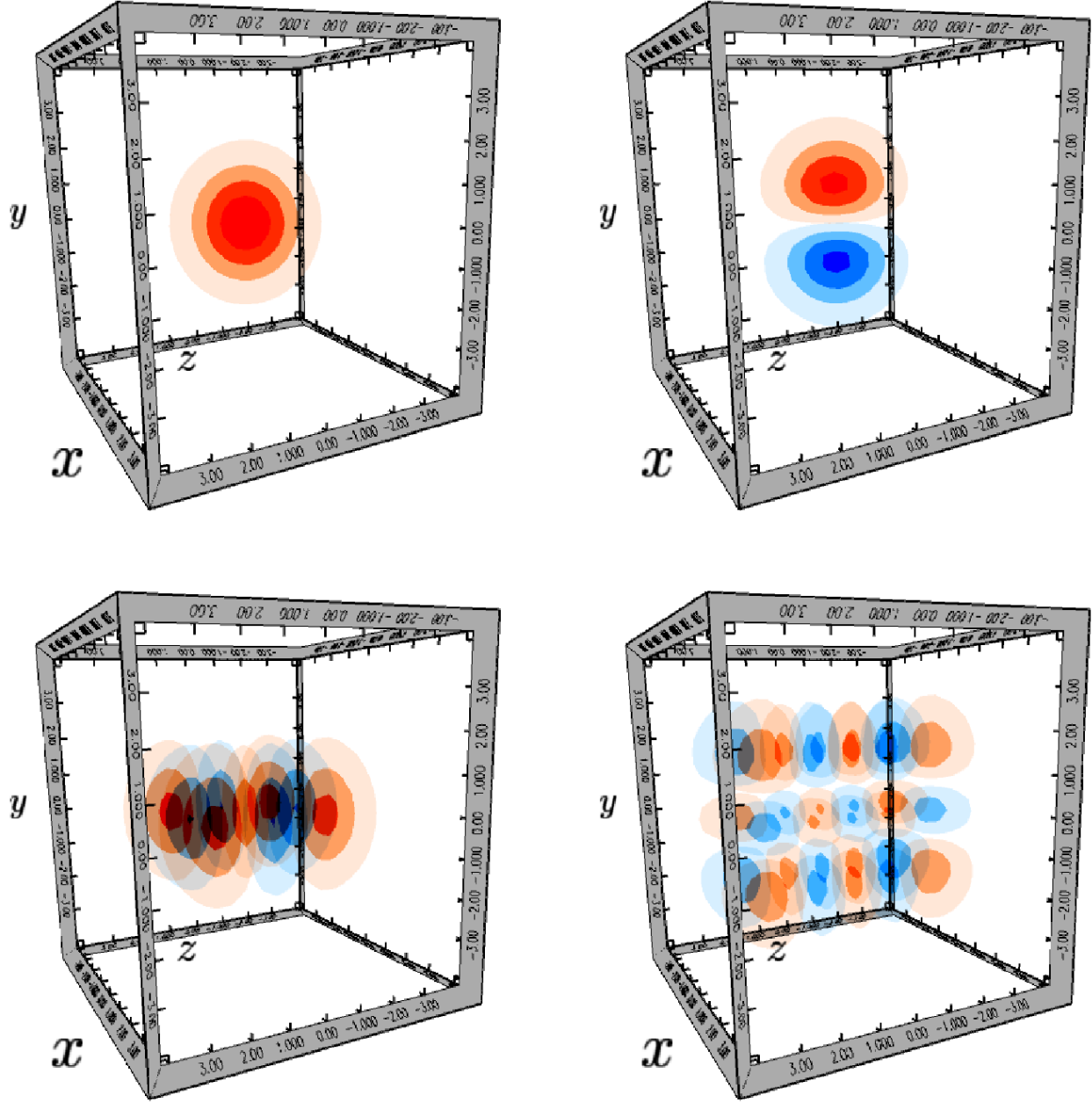


Figure 1. Examples of three-dimensional Cartesian shapelets ($\beta = 1$). Top row: (left) $\mathbf{n} = (0, 0, 0)$; (right) $\mathbf{n} = (0, 1, 0)$. Bottom row: (left) $\mathbf{n} = (2, 0, 2)$; (right) $\mathbf{n} = (1, 2, 4)$. For each panel, we calculate the maximum data value, f_{\max} , and generate 10 equally spaced iso-surfaces over the range $(-f_{\max}, f_{\max})$. Individual isosurfaces are coloured with a two-ended intensity colour map: blue \rightarrow black \rightarrow orange.

with $\mathbf{x} = (x_1, x_2)$ and $\mathbf{n} = (n_1, n_2)$. Consequently, the extension to 3-d Cartesian shapelets is now almost trivial:

$$B_{3,\mathbf{n}}(\mathbf{x}; \beta) \equiv \beta^{-3/2} \phi_{3,\mathbf{n}}(\beta^{-1} \mathbf{x}). \quad (11)$$

where

$$\phi_{3,\mathbf{n}}(\mathbf{x}) \equiv \phi_{n_1}(x_1) \phi_{n_2}(x_2) \phi_{n_3}(x_3) \quad (12)$$

with $\mathbf{x} = (x_1, x_2, x_3)$ and $\mathbf{n} = (n_1, n_2, n_3)$. The 3-d Cartesian shapelet coefficients have the form:

$$f_{3,\mathbf{n}} = \int_V f_3(\mathbf{x}) B_{3,\mathbf{n}}(\mathbf{x}; \beta) d^3x \quad (13)$$

with the integration occurring over the infinite volume of the domain, V , and the 3-dimensional shapelet decomposition is:

$$f_3(\mathbf{x}) = \sum_{n_1, n_2, n_3} f_{3,\mathbf{n}} B_{3,\mathbf{n}}(\mathbf{x}; \beta). \quad (14)$$

We present examples of 3-d Cartesian shapelets in Fig. 1, using equally-spaced isosurfaces, and a two-ended intensity colour-map ranging from blue (negative values) to black (zero) to orange (positive values).

Two further useful quantities are the characteristic radius of a 3-d shapelet:

$$\theta_{3,\max} \approx \beta (n_{\max} + 3/2)^{1/2}, \quad (15)$$

and the size of small scale oscillatory features:

$$\theta_{3,\min} \approx \beta (n_{\max} + 3/2)^{-1/2}. \quad (16)$$

These expressions are based on well known quantum mechanics results for the QHO, and are the 3-d versions of the expressions presented in Refregier (2003). They provide a starting point for determining appropriate decomposition parameters, as discussed in Section 4.2.

2.3 d -dimensional Cartesian shapelets

It is straightforward to infer that the d -dimensional generalisation of the shapelet basis functions is:

$$B_{d,\mathbf{n}}(\mathbf{x}; \beta) \equiv \beta^{-d/2} \phi_{d,\mathbf{n}}(\beta^{-1}\mathbf{x}) \quad (17)$$

with

$$\phi_{d,\mathbf{n}}(\mathbf{x}) \equiv \prod_{i=1}^d \phi_{n_i}(x_i). \quad (18)$$

We can then write a general orthonormality condition:

$$\int_V B_{d,\mathbf{n}}(\mathbf{x}; \beta) B_{d,\mathbf{m}}(\mathbf{x}; \beta) d^d x = \prod_{i=1}^d \delta_{n_i m_i}, \quad (19)$$

the shapelet coefficients have the form:

$$f_{d,\mathbf{n}} = \int_V f_d(\mathbf{x}) B_{d,\mathbf{n}}(\mathbf{x}; \beta) d^d x \quad (20)$$

and the d -dimensional shapelet decomposition is:

$$f_d(\mathbf{x}) = \sum_{n_1, n_2, \dots, n_d=0}^{\infty} f_{d,\mathbf{n}} B_{d,\mathbf{n}}(\mathbf{x}; \beta). \quad (21)$$

In d -dimensions, the characteristic sizes are:

$$\theta_{d,\max} \approx \beta (n_{\max} + d/2)^{1/2} \quad (22)$$

and

$$\theta_{d,\min} \approx \beta (n_{\max} + d/2)^{-1/2}. \quad (23)$$

We note that Coffey (2006) refers to the d -dimensional solutions of the harmonic oscillator, but does not present specific d -dimensional results in the form we use.

3 ANALYTIC EXPRESSIONS

Refregier (2003) demonstrates how analytic expressions can be obtained for common properties of 2-d images. We now derive analytic expressions for physical properties of 3-d structures using 3-d Cartesian shapelets, and their generalisation to d -dimensions.

3.1 Zeroth moment

The zeroth moment, M_0 , of an arbitrary (well-behaved) function, $f_3(\mathbf{x})$, in three dimensions is

$$M_0 \equiv \int_V f_3(\mathbf{x}) d^3 x. \quad (24)$$

Writing this in terms of the shapelet coefficients, using equation (14), and the orthonormality condition, equation (6):

$$M_0 = \sum_{n_1, n_2, n_3} f_{3,\mathbf{n}} \int_{-\infty}^{\infty} B_{n_1} dx_1 \int_{-\infty}^{\infty} B_{n_2} dx_2 \int_{-\infty}^{\infty} B_{n_3} dx_3 \quad (25)$$

$$= \pi^{3/4} \beta^{3/2} \sum_{n_1, n_2, n_3}^{\text{even}} f_{3,\mathbf{n}} U_{3,\mathbf{n}} W_{3,\mathbf{n}}, \quad (26)$$

where

$$U_{n_1, n_2, n_3} \equiv 2^{(3-n_1-n_2-n_3)/2}, \quad (27)$$

and

$$W_{n_1, n_2, n_3} \equiv \left[\begin{pmatrix} n_1 \\ n_1/2 \end{pmatrix} \begin{pmatrix} n_2 \\ n_2/2 \end{pmatrix} \begin{pmatrix} n_3 \\ n_3/2 \end{pmatrix} \right]^{1/2}, \quad (28)$$

are factors that recur in the analytic expressions to follow. We have used the integral property [see equation (17) of Refregier (2003)] for even n :

$$J_n \equiv \int_{-\infty}^{\infty} B_n(x; \beta) dx = \left(2^{1-n} \pi^{1/2} \beta \right)^{1/2} \begin{pmatrix} n \\ n/2 \end{pmatrix}^{1/2}, \quad (29)$$

while for odd n , the integrals in equation (25) vanish as $B_n(\mathbf{x}; \beta)$ is an odd function.

For applications in image processing, Refregier (2003) identifies total flux, F , with the 2-d zeroth moment. In 3-d, a more natural association might be made with total mass, M , for an object with density field, $f_3(\mathbf{x}) = \rho(\mathbf{x})$.

3.2 Centroid

The centroid position of a 3-d object is:

$$\hat{x}_i \equiv \frac{1}{M_0} \int_V x_i f_3(\mathbf{x}) d^3 x \quad (30)$$

for $i = 1, 2, 3$. The orthonormality condition enables us to write the series expansion as (for clarity, we only show results for \hat{x}_1):

$$\hat{x}_1 = \frac{1}{M_0} \sum_{n_1, n_2, n_3} f_{3,\mathbf{n}} J_{n_2} J_{n_3} \int_{-\infty}^{\infty} x_1 B_{n_1} dx_1. \quad (31)$$

Using the recursion relation, equation (A3), and the fact that

$$\int_{-\infty}^{\infty} \frac{dB_{n_i}}{dx_i} dx_i = 0, \quad (32)$$

gives the intermediate result

$$\hat{x}_1 = \frac{\sqrt{2}\beta}{M_0} \sum_{n_1, n_2, n_3} f_{3,\mathbf{n}} J_{n_2} J_{n_3} \int_{-\infty}^{\infty} \sqrt{n_1 + 1} B_{n_1+1} dx_1. \quad (33)$$

With the notation introduced above, we have

$$\hat{x}_1 = \frac{\pi^{3/4} \beta^{5/2}}{M_0} \sum_{n_1}^{\text{odd}} \sum_{n_2, n_3}^{\text{even}} f_{3,\mathbf{n}} \sqrt{n_1 + 1} U_{n_1, n_2, n_3} W_{n_1+1, n_2, n_3} \quad (34)$$

and similar results for \hat{x}_2 and \hat{x}_3 .

3.3 Root-mean-square radius

The root-mean-square (RMS) radius of a 3-d object is:

$$r_{\text{RMS}}^2 \equiv \frac{1}{M_0} \int_V x^2 f_3(\mathbf{x}) d^3x, \quad (35)$$

where $x = |\mathbf{x}| = \sqrt{x_1^2 + x_2^2 + x_3^2}$, gives an estimate of the physical extent of the object under investigation. Substituting equation (14) into the above, and using equation (6):

$$r_{\text{RMS}}^2 = \frac{1}{M_0} \sum_{n_1, n_2, n_3}^{\text{even}} f_{3, \mathbf{n}} \left[J_{n_2} J_{n_3} \int_{-\infty}^{\infty} x_1^2 B_{n_1} dx_1 \right. \\ \left. + J_{n_1} J_{n_3} \int_{-\infty}^{\infty} x_2^2 B_{n_2} dx_2 + J_{n_1} J_{n_2} \int_{-\infty}^{\infty} x_3^2 B_{n_3} dx_3 \right] \quad (36)$$

From equation (A4) and noting that

$$\int_{-\infty}^{\infty} \frac{d^2 B_{n_i}}{dx_i^2} dx_i = 0, \quad (37)$$

we have

$$r_{\text{RMS}}^2 = \frac{2\pi^{3/4} \beta^{7/2}}{M_0} \sum_{n_1, n_2, n_3}^{\text{even}} f_{3, \mathbf{n}} (n_1 + n_2 + n_3 + 3/2) \\ \times U_{n_1, n_2, n_3} W_{n_1+1, n_2+1, n_3}. \quad (38)$$

3.4 Quadrupole moment tensor

The quadrupole moment tensor is:

$$Q_{ij} \equiv \int_V f_3(\mathbf{x}) (3x_i x_j - x^2 \delta_{ij}) d^3x, \quad (39)$$

which is symmetric and traceless, so that there are only five independent elements. Performing the same calculations as in the previous section, the diagonal components of the quadrupole moment tensor are:

$$Q_{11} = 2\pi^{3/4} \beta^{7/2} \sum_{n_1, n_2, n_3}^{\text{even}} f_{3, \mathbf{n}} (2n_1 - n_2 - n_3) U_{n_1, n_2, n_3} W_{n_1, n_2, n_3}. \quad (40)$$

Q_{22} and Q_{33} have a similar form. The off-diagonal components are

$$Q_{12} = 3\pi^{3/4} \beta^{7/2} \sum_{n_1, n_2}^{\text{odd}} \sum_{n_3}^{\text{even}} f_{3, \mathbf{n}} \sqrt{(n_1 + 1)(n_2 + 1)} \\ \times U_{n_1, n_2, n_3} W_{n_1+1, n_2+1, n_3} \quad (41)$$

and similarly for the other Q_{ij} with $i \neq j$.

3.5 Moment of inertia tensor

For the special case where $f_3(\mathbf{x}) = \rho(\mathbf{x})$ represents a mass-density field, we can calculate the moments of inertia. The moment of inertia tensor describes all moments of inertia of an object about different axes of rotation, usually calculated with respect to the centre of mass of the object. In component form:

$$I_{ij} \equiv \int_V f_3(\mathbf{x}) (x^2 \delta_{ij} - x_i x_j) d^3x. \quad (42)$$

In coefficient space, the diagonal elements of the inertia tensor are:

$$I_{11} = 2\pi^{3/4} \beta^{7/2} \sum_{n_1, n_2, n_3}^{\text{even}} f_{3, \mathbf{n}} (n_2 + n_3 + 1) U_{n_1, n_2, n_3} W_{n_1, n_2, n_3} \quad (43)$$

and similarly for I_{22} and I_{33} . The off-diagonal elements are

$$I_{12} = -\pi^{3/4} \beta^{7/2} \sum_{n_1, n_2}^{\text{odd}} \sum_{n_3}^{\text{even}} f_{3, \mathbf{n}} \sqrt{(n_1 + 1)(n_2 + 1)} \\ \times U_{n_1, n_2, n_3} W_{n_1+1, n_2+1, n_3} \quad (44)$$

and similarly for the remaining elements.

3.6 Transformations

Refregier (2003) demonstrates how shapelet coefficients are modified under a general coordinate transformation in terms of a set of operators generating rotation, convergence, shear and translation. As we have not used the operator formulation explicitly elsewhere in the present work, we choose not to introduce this approach now. Instead, we treat simple coordinate transformations in terms of a modification of the integral in equation (13).

Consider an arbitrary (small) coordinate transformation:

$$\mathbf{x} \rightarrow \mathbf{x}' = (1 + \Psi)\mathbf{x} + \epsilon \quad (45)$$

where ϵ is a translation, and Ψ is a 3×3 transformation matrix. To obtain the shapelet coefficients of the transformed input shape, $f_{3, \mathbf{n}}^T$, we must solve the integral:

$$f_{3, \mathbf{n}}^T \simeq \int_V f_3(\mathbf{x} - \Psi\mathbf{x} - \epsilon) B_{3, \mathbf{n}}(\mathbf{x}; \beta) d^3x \quad (46)$$

for each \mathbf{n} , which is first order in Ψ . We introduce transformed coordinates, and a new set of shapelet basis functions,

$$B_{3, \mathbf{n}}(\mathbf{x}; \beta) \rightarrow B_{3, \mathbf{n}}(\mathbf{x}' - \Psi\mathbf{x}' - \epsilon). \quad (47)$$

In general, the relevant integral expressions for transformed coordinates must be calculated numerically. We can gain insight into the effect of simple transformations by considering the effect of translations and dilations on the shapelet ground state, $B_{3, \mathbf{n}=(0,0,0)}(\mathbf{x}; \beta)$.

3.6.1 Translation

The effect of a (small) translation, $\epsilon = (\epsilon_1, \epsilon_2, \epsilon_3)$, on the shapelet coefficients is:

$$f_{3, \mathbf{n}}^T \simeq \int_{V'} f_3(\mathbf{x}') B_{3, \mathbf{n}}(\mathbf{x} - \epsilon) d^3x'. \quad (48)$$

As an example, we solve this for the \mathbf{n} -tuples: $(0, 0, 0)$, $(1, 0, 0)$ and $(2, 0, 0)$, to find:

$$f_{3, \mathbf{n}=(0,0,0)}^T = e^{-\epsilon_1^2/4\beta^2} e^{-\epsilon_2^2/4\beta^2} e^{-\epsilon_3^2/4\beta^2} \quad (49)$$

$$f_{3, \mathbf{n}=(1,0,0)}^T = -\frac{\epsilon_1}{\beta\sqrt{2}} e^{-\epsilon_1^2/4\beta^2} e^{-\epsilon_2^2/4\beta^2} e^{-\epsilon_3^2/4\beta^2} \quad (50)$$

$$f_{3, \mathbf{n}=(2,0,0)}^T = \frac{\epsilon_1^2}{\beta^2\sqrt{2}} e^{-\epsilon_1^2/4\beta^2} e^{-\epsilon_2^2/4\beta^2} e^{-\epsilon_3^2/4\beta^2}. \quad (51)$$

$$(52)$$

As expected, shapelet power is transformed from the ground state to higher-order shapelet terms. In all cases, if any of the $\epsilon_i = 0$, then the orthonormality condition, equation (6), prevails.

3.6.2 Dilation

Next, we consider a transformation that is a pure dilation:

$$\Psi = \kappa = \begin{pmatrix} \kappa_1 & 0 & 0 \\ 0 & \kappa_2 & 0 \\ 0 & 0 & \kappa_3 \end{pmatrix} \quad (53)$$

where all the $|\kappa_i| \ll 1$. Transformed shapelet coefficients are:

$$f_{3,\mathbf{n}}^T \simeq \frac{\int_V f_3(\mathbf{x}') B_{3,\mathbf{n}}(\mathbf{x}' - \Psi \mathbf{x}') d^3 \mathbf{x}'}{(1 + \kappa_1)(1 + \kappa_2)(1 + \kappa_3)} \quad (54)$$

Using the ground state shapelet and the same \mathbf{n} -tuples as previously, we find:

$$f_{3,\mathbf{n}=(0,0,0)}^T = 2^{3/2} [2 + \kappa_1(2 + \kappa_1)]^{-1/2} \times [2 + \kappa_2(2 + \kappa_2)]^{-1/2} [2 + \kappa_3(2 + \kappa_3)]^{-1/2} \quad (55)$$

$$f_{3,\mathbf{n}=(1,0,0)}^T = 0 \quad (56)$$

$$f_{3,\mathbf{n}=(2,0,0)}^T = 2\kappa_1(2 + \kappa_1) [2 + \kappa_1(2 + \kappa_1)]^{-3/2} \times [2 + \kappa_2(2 + \kappa_2)]^{-1/2} [2 + \kappa_3(2 + \kappa_3)]^{-1/2} \quad (57)$$

Since the ground state is a symmetric shape, under a dilation, the odd shapelet coefficients vanish.

3.6.3 Rotations

The same approach can be used for rotations about the coordinate axes, which are defined in terms of the standard 3×3 rotation matrices of the form:

$$\mathbf{R}_1(\theta_1) = \begin{pmatrix} 1 & 0 & 0 \\ 0 & \cos \theta_1 & -\sin \theta_1 \\ 0 & \sin \theta_1 & \cos \theta_1 \end{pmatrix}, \quad (58)$$

and similarly for rotations about the x_2 -axis, $\mathbf{R}_2(\theta_2)$, and x_3 -axis, $\mathbf{R}_3(\theta_3)$. A sequence of rotations can be combined into a single general rotation matrix, $\mathbf{R}_x(\boldsymbol{\theta})$. The coordinate transformations for rotations are tractable but more complex algebraically than for translations and dilations – equations (48) and (54). Rather than providing a general analytic form for the rotations, we instead demonstrate the resulting change in amplitude of shapelet coefficients under an arbitrary rotation in Section 5.2, in particular Figs. 6–8.

3.7 d -dimensional expressions

We can use the results from the previous sub-sections to obtain analytic expressions in d -dimensions. The zeroth moment is:

$$M_0 = \pi^{d/4} \beta^{d/2} \sum_{\mathbf{n}_1, \mathbf{n}_2, \dots, \mathbf{n}_d}^{\text{even}} f_{d,\mathbf{n}} U_{d,\mathbf{n}} W_{d,\mathbf{n}} \quad (59)$$

where now

$$U_{n_1, n_2, \dots, n_d} = 2^{\frac{1}{2}(d - \sum_{i=1}^d n_i)} \quad (60)$$

and

$$W_{n_1, n_2, \dots, n_d} = \left[\prod_{i=1}^d \binom{n_i}{n_i/2} \right]^{1/2}. \quad (61)$$

The centroid is:

$$\hat{x}_1 = \frac{\pi^{d/4} \beta^{(d+2)/2}}{M_0} \sum_{n_1}^{\text{odd}} \sum_{n_2, \dots, n_d}^{\text{even}} f_{d,\mathbf{n}} \sqrt{(n_1 + 1)} \times U_{n_1, n_2, \dots, n_d} W_{n_1+1, n_2, \dots, n_d}, \quad (62)$$

and similarly for $\hat{x}_2, \dots, \hat{x}_d$. Finally, with $x = |\mathbf{x}| = \sqrt{x_1^2 + x_2^2 + \dots + x_d^2}$, we have the d -dimensional RMS radius:

$$r_{\text{RMS}}^2 = \frac{2\pi^{d/4} \beta^{2+d/2}}{M_0} U_{n_1, \dots, n_d} W_{n_1, \dots, n_d} \times \sum_{n_1, \dots, n_d}^{\text{even}} f_{d,\mathbf{n}} \left(n_1 + n_2 + \dots + n_d + \frac{d}{2} \right). \quad (63)$$

We do not attempt to derive d -dimensional equivalents of the quadrupole moment or moment of inertia tensors, as these are more natural quantities in three-dimensions. However, the generalised approach we have demonstrated can be applied to other properties defined as d -dimensional integrals of $f_d(\mathbf{x})$.

4 IMPLEMENTATION ISSUES

Before we can use the analytic expressions of Section 3 to study three-dimensional objects, we need to obtain the shapelet coefficients. In this section, we discuss some of the issues in implementing an efficient 3-d shapelet decomposition code.

4.1 Voxellation

In applications to image simulation (Massey et al. 2004; Young et al. 2005) and gravitational lensing (Refregier & Bacon 2003; Goldberg & Bacon 2005; Kuijken 2006), shapelet quantities are calculated for a pixel grid of image intensities, which is often obtained as a ‘postage stamp’ region selected from a larger image. For the 3-d case, we use a regular cubic mesh of voxels (volume elements).

The discrete sampling of the 3-d structure onto a mesh means we need to integrate each shapelet term over the physical size of a voxel, under the assumption that the data value in the voxel is constant. This is valid for data that is already on a grid (e.g. from a mesh-based simulation), and can be achieved for point-based data by smoothing to the grid with an appropriate smoothing scheme.

For integration over a finite cubic volume, \hat{V} , over spatial range x_{\min} to x_{\max} (and similarly for y and z), equation (13) is replaced by a summation over N_g^3 voxels:

$$f_{3,\mathbf{n}} = \sum_{i,j,k}^{N_g, N_g, N_g} f_{ijk} \int_{\hat{V}_{ijk}} B_{\mathbf{n}}(\mathbf{x}) d^3 \mathbf{x} \quad (64)$$

where our grid-based 3-d shape has a constant value in each voxel, f_{ijk} . The volume is assumed to be sufficiently large that the $f_{ijk} \rightarrow 0$ outside of the integration region.

Following Massey & Refregier (2005), the orthonormality of shapelets means we can simplify the per-voxel integration of the shapelet term as the product of three one-dimensional integrals of the form:

$$I_n(i) = \int_a^b B_n(x) dx. \quad (65)$$

where the index, $1 \leq i \leq N_g$, specifies the one-dimensional voxel coordinate, and hence the integration limits on the boundaries of the i th voxel are:

$$a = x_{\min} + (i-1)\Delta x \quad (66)$$

$$b = a + \Delta x, \quad (67)$$

with cell width

$$\Delta x = \frac{x_{\max} - x_{\min}}{N_g}. \quad (68)$$

This allows us to write equation (64) as a sum over all voxels:

$$f_{3,\mathbf{n}} = \sum_{i,j,k}^{N_g, N_g, N_g} f_{ijk} I_{n_1}(i) I_{n_2}(j) I_{n_3}(k) \quad (69)$$

providing a set of shapelet coefficients that are used to calculate the analytic quantities of Section 3.

Equation (65) has recursion solutions²

$$I_n(i) = -\beta \sqrt{\frac{2}{n}} [B_{n-1}(x)]_a^b + \sqrt{\frac{n-1}{n}} I_{n-2}(i) \quad (70)$$

with

$$I_0(i) = \sqrt{\frac{\beta \pi^{1/2}}{2}} \left[\operatorname{erf} \left(\frac{x}{\beta \sqrt{2}} \right) \right]_a^b \quad (71)$$

$$I_1(i) = -\beta \sqrt{2} [B_0(x)]_a^b. \quad (72)$$

4.2 Optimal decomposition

A key problem is the choice of parameters, $(\beta, n_{\max}, \mathbf{x}_c)$, to perform an optimal shapelet decomposition. We use the notation \mathbf{x}_c to refer to the best-fitting object centroid, as opposed to the shapelet reconstructed value, $\hat{\mathbf{x}}$. A good choice of parameters will ensure compact representation of the original data in coefficient space, while retaining high accuracy. Well chosen parameters will also exclude any noise that may be present in the data. As Melchior et al. (2007) highlighted for the 2-d case, shapelet decompositions may appear good visually, so it is important to define an appropriate goodness of fit, particularly as shapelet space can be highly degenerate.

The β parameter is the characteristic scale of the object to be decomposed. Increasing β has the effect of increasing the amplitude of the shapelets and dilating them along all coordinate axes. Changing the amplitude of the shapelets has no effect on the optimisation as the obtained coefficients simply scale in proportion to the change in amplitude, i.e. β is a one-dimensional spatial parameter.

The maximum number of coefficients needed relates to the complexity of the data. A value of n_{\max} that is too low will likely result in loss of information regarding the smallest features; if n_{\max} is too high, noise and arbitrary high-frequency variations will be reproduced. Moreover, with increasing n_{\max} , the range of β and \mathbf{x}_c values that give viable solutions increases. This is because the additional coefficients can compensate for a poor choice of β and \mathbf{x}_c . It is therefore important that a minimum optimal n_{\max} value

is used, while not resulting in significant loss of structural information, along with the optimal β and \mathbf{x}_c values.

To determine appropriate n_{\max} and β values, we solve for the two unknown quantities in equations (15) and (16):

$$n_{\max} = \frac{\theta_{3,\max}}{\theta_{3,\min}} - \frac{3}{2} \quad (73)$$

and

$$\beta = \sqrt{\theta_{3,\max} \theta_{3,\min}}. \quad (74)$$

Consider a voxel grid centred on the coordinate origin with major axis length, $x_{\max} = -x_{\min}$, which is taken to be twice the maximum particle distance, $\theta_{3,\max}$, from the coordinate origin. In this case, the cell width is:

$$\Delta x = \frac{2x_{\max}}{N_g}. \quad (75)$$

Choosing $\theta_{3,\min} = \Delta x/2$, it follows that

$$n_{\max} = (N_g - 3)/2 \quad (76)$$

and

$$\beta = x_{\max} / \sqrt{2N_g}. \quad (77)$$

For specific applications, convergence studies may be a more appropriate way to select initial estimates for n_{\max} and β , and the size of the data ‘padding’ region.

To minimise the number of evaluations, and avoid some of the issues of generating shapelet coefficients with too many orders, we impose the constraint [see Section 3.1 of Refregier (2003)]:

$$0 \leq (n_1 + n_2 + n_3) \leq n_{\max}. \quad (78)$$

This constraint means that the total number of shapelet terms to be evaluated for a given n_{\max} is:

$$N_{\text{eval}} = \frac{1}{6} (n_{\max} + 1)(n_{\max} + 2)(n_{\max} + 3). \quad (79)$$

This last equation is the $d = 3$ version of the more general result:

$$N_{\text{eval}} = \binom{n_{\max} + d}{d} \quad (80)$$

to obtain the unique set of \mathbf{n} values satisfying:

$$0 \leq \sum_m^d n_m \leq n_{\max}. \quad (81)$$

Coefficient-based measurements may produce inaccurate results in cases when the chosen n_{\max} , β and \mathbf{x}_c values result in a reconstructed shape that is truncated by the bounding cube of the original data grid (in other words, when the reconstructed shape is bigger than the original data). Ensuring that the parameter bounds previously outlined are not traversed, i.e. through the use of the padding region, will prevent this from occurring. Moreover, estimates of the $\hat{\mathbf{x}}$ and r_{RMS}^2 may fail if $M_0 = 0$, since they depend on the reciprocal of the zeroth moment. This may occur for values of β that are too large.

Further discussion of strategies for optimal shapelet decomposition are beyond the scope of this paper – see Massey & Refregier (2005) for an approach based on the steepest descent method. We now investigate the decomposition process from an algorithmic viewpoint, and consider opportunities

² There is an error in the factors of β in equation (32) of Massey & Refregier (2005), which is corrected in the arXiv version of their paper: arXiv:astro-ph/0408445.

for accelerating the computation of shapelet coefficients using graphics processing units.

4.3 Algorithmic considerations

The algorithm for obtaining a shapelet decomposition for a voxellated structure is:

- (i) Choose the target grid resolution, N_g , and desired n_{\max} , which constrain the initial choice of β .
- (ii) Generate an array of shapelet amplitude estimates, $f_{3,\mathbf{n}}$, with N_{eval} entries (i.e. the minimum number that must be calculated), and initialise to zero-values.
- (iii) Calculate the 1-dimensional $I_n(i)$ terms for all orders up to n_{\max} , resulting in $n_{\max}N_g$ stored values of $I_n(i)$.
- (iv) Loop over the elements of the \mathbf{n} vector, subject to the constraint of equation (78), then:

- (a) For each set of \mathbf{n} values, loop over N_g^3 cells with indices (i, j, k) and calculate the quantity:

$$f_{3,\mathbf{n}} := f_{3,\mathbf{n}} + I_{n_1}(i) \times I_{n_2}(j) \times I_{n_3}(k) \times f_{ijk}. \quad (82)$$

- (v) Output the shapelet amplitudes for further processing and analysis.

The process for reconstructing a three-dimensional shape from its shapelet coefficients proceeds as follows:

- (i) Create an empty shape, $\hat{f}_3(\mathbf{x})$, with dimensions N_g^3 , and zero all \hat{f}_{ijk} values.
- (ii) Loop over \mathbf{n} vector, subject to constraint of equation (78), calculating:

$$\hat{f}_3(\mathbf{x}) := \hat{f}_3(\mathbf{x}) + B_{3,\mathbf{n}}(\mathbf{x}; \beta). \quad (83)$$

An optional filter can be applied in the reconstruction by only adding the contributions from shapelet terms where $f_{3,\mathbf{n}}$ meets a prescribed criteria. Such an approach may be useful for removing noise, or to investigate the dependence of the analytic solutions on a particular shapelet order – see the example application in Section 5.3.

Obtaining a shapelet decomposition of a voxellated structure involves computing equation (69) for all N_{eval} coefficients. This computation is both very regular and abundant in inherent parallelism – two traits that suggest a strong suitability for implementation on many-core computing architectures such as graphics processing units (GPUs).

GPUs were originally developed to accelerate the rendering of three-dimensional graphics through the use of a custom processor with a highly parallel architecture. GPUs are now capable of supporting general (i.e. non-graphics) computations through the use of software platforms such as the Compute Unified Device Architecture (CUDA) from NVIDIA³ or implementations of the OpenCL⁴ standard.

We can assess the suitability of the shapelet algorithm for a GPU implementation by using an algorithm analysis approach similar to that of Barsdell, Barnes & Fluke (2010), who noted that the most important considerations for an algorithm on a GPU are: massive parallelism, branching, arithmetic intensity and memory access patterns. To begin

with, we assess the amount of parallelism in the shapelet decomposition problem. For simplicity, we assume that data is placed inside a bounding box such that all of the dimensions are the same – if there are fewer grid points along one axis, these must be zero-padded to the maximum grid scale.

The computation of equation (69) involves a summation over the three coordinate dimensions, i, j, k , for each shapelet coefficient defined by n_1, n_2, n_3 . The computation over n_1, n_2, n_3 is therefore entirely (or *embarrassingly*) parallel, as each coefficient can be computed independently. The summation over voxels also exhibits inherent parallelism, but requires some coordination between elements. For this reason we will first consider parallelising the shapelet algorithm only over the shapelet coefficients, and will assume the summations are performed sequentially.

Parallelising the problem over the shapelet coefficients defined by n_1, n_2, n_3 allows a maximum of N_{eval} parallel *threads* to work on the problem simultaneously. For $n_{\max} = 20$, this is 1771 threads. While this is likely to exceed the number of physical processor cores in any current hardware architecture, modern GPUs often require an order of magnitude more threads in flight before their full potential is reached. It is therefore likely that some of the summation will need to be parallelised in addition to the evaluation of the shapelet coefficients. One such approach would be to compute sums over slices of the data volume in parallel, before combining them in a second stage of computation. This would increase the number of threads by a factor of N_g , which would almost certainly saturate the available hardware performance.

The next concern is branching, which occurs when parallel threads execute differing instructions as a result of a conditional statement. Besides the application of the constraint $n_1 + n_2 + n_3 < n_{\max}$, the shapelet decomposition algorithm does not require any branching operations. We therefore conclude that this factor will not significantly influence performance on a GPU.

Arithmetic intensity is the ratio of arithmetic operations to memory-access operations. A high arithmetic intensity means that the GPU's instruction hardware will be fully utilised; a low intensity means that getting data from memory to the processors will be a bottle-neck and performance will be limited. The total input data to the shapelet algorithm scales as $O(N_g^3)$, while the computation scales as $O(N_{\text{eval}}N_g^3)$. This implies a very high theoretical peak arithmetic intensity of $O(N_{\text{eval}}) \approx O(1000)$. This would be achieved by re-using input data f_{ijk} for the computation of many n_1, n_2, n_3 values. Assuming such behaviour could be effected, the performance would be limited by the arithmetic throughput of the hardware, and we would expect to see very good performance on a GPU.

In practice, the re-use of data is achieved through the exploitation of a *cache*, which is an area of very fast memory in which small amounts of data can be stored. On NVIDIA GPUs, the specific cache we refer to is known as *shared memory*. By loading a block of f_{ijk} data into shared memory, threads can re-use the data multiple times before having to load another block in. As all of the operations on the input data f_{ijk} scale as $O(N_g^3)$, there is no difference between caching a block of any particular shape; for simplicity we therefore consider caching a simple one-dimensional block of data in the i dimension. In this setup, the j and k indices

³ http://www.nvidia.com/object/cuda_home_new.html

⁴ <http://www.khronos.org/opencl/>

can remain constant during the computation of the block, which allows the value $I_{n_2}(j)I_{n_3}(k)$ to be pre-computed and stored locally before computation of the block begins. If, in addition, the value of n_1 is made to remain constant over the local group of threads, then the values $f_{ijk}I_{n_1}(i)$ can be pre-computed and stored in shared memory. The computation by each thread of the block of i values then only involves the multiplication and accumulation of two pre-computed values. Multiplication followed by addition also happens to be the fastest operation available on current GPU hardware.

The last concern is the memory access pattern exhibited by the algorithm. Fortunately, the regularity of the computation means that data are typically accessed in an aligned and contiguous fashion, and there should therefore be no issues in achieving a high memory throughput.

To reduce the computational overhead in the evaluation of equation (69), the integrals I_n can be pre-computed once for each input shape and stored in look-up tables. The recursion relation, equation (70), makes it practical to evaluate and store *all* shapelet orders up to n_{\max} for N_g grid cells along one dimension. This involves only $O(n_{\max}N_g)$ terms, and could be computed on the CPU without impacting on the overall performance of the algorithm. A further advantage of using the recursion relations is that sufficient numerical precision can be maintained, even for high n values. If we calculated each shapelet term independently from equation (2), then the pre-factors, $(2^n n!)^{-1/2}$ tend to zero very rapidly, and for $n > 30$, cannot be stored sufficiently accurately in single precision. This requirement is of relevance to GPU implementation, as the greatest processing speed-ups offered by the current generation of GPUs is for single precision, and reduces the overall memory required by storing as 32-bit rather than 64-bit values.

Given the strong degree of parallelism exhibited by the algorithm, the ability to efficiently cache the input data and take advantage of a very high arithmetic intensity, the ability to pre-compute the shapelet integral terms, and the fact that the core of the algorithm can be reduced to simple multiply-add operations, we conclude that an implementation of the shapelet decomposition algorithm on a GPU would likely achieve a level of performance very near the peak capability of the hardware. Shapelet decomposition thus stands to benefit significantly from current trends in commodity computing hardware, and may have an additional advantage over related methods that are unable to take advantage of massively-parallel architectures.

The extension of the above algorithm analysis to d -dimensional shapelet decompositions should be straightforward, and we expect the conclusions to remain unchanged; however, implementation complexity is likely to increase, particularly in the general case.

For the application domain we now explore, viz. 3-d Cartesian shapelet representations of simulated dark matter haloes, we have used a CPU-only implementation of the decomposition algorithm.

5 THE SHAPES OF DARK MATTER HALOES

If the only use of the shapelet approach was to calculate the analytic expressions of Section 3, then it would be a somewhat inefficient one, compared to direct numerical integra-

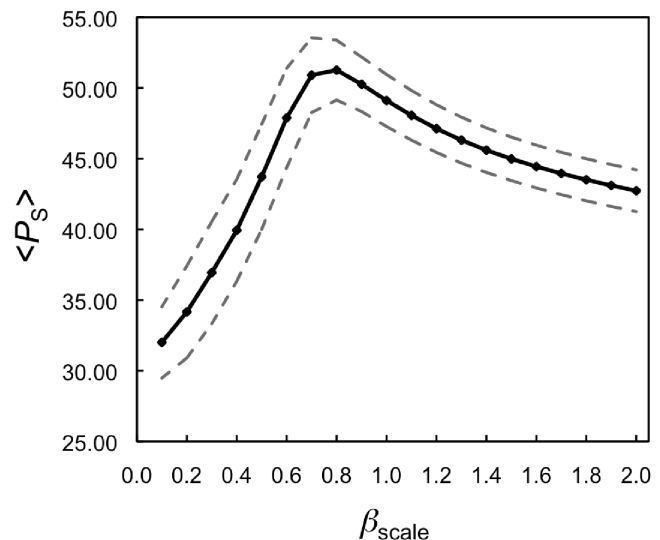


Figure 2. To select an appropriate β_{scale} for classification of halo shapes, we calculate the average peak signal-to-noise ratio, $\langle P_S \rangle$, over 200 input haloes (markers; black solid line). Dashed lines represent the one-standard deviation error range. On the basis of this analysis, we choose $\beta_{\text{scale}} = 0.8$, which presents a reasonable compromise to a full optimisation process.

tion of equations (24), (30), (35), (39), and (42). The benefit of the shapelet decomposition is that we now have additional information concerning the shape. Opportunities for classifying three-dimensional structures based on the shapelet terms may be made through identification of the dominant shapelet terms, or by investigating relative weights of particular shapelet orders. In this section, we demonstrate how three-dimensional shapelet analysis of dark matter haloes suggests a new method for automatically classifying halo types.

5.1 Shapes and sub-structure

For some time, it has been known that Cold Dark Matter (CDM) cosmologies predict the formation of triaxial haloes (on average), with a slight preference for prolate haloes over oblate ones (Davis et al. 1985; Barnes & Efstathiou 1987; Frenk et al. 1988; Dubinski & Carlberg 1991; Dubinski 1994; Cole & Lacey 1996; Jing & Suto 2002; Kasun & Evrard 2005; Bailin & Steinmatz 2005; Oguri et al. 2005; Allgood et al. 2006; Knebe & Wiefner 2006; Kuhlen, Diemand & Madau 2007). These studies include measuring the distribution of halo triaxialities, studying the effects of baryons (which tend to reduce the triaxiality compared to dark matter only models), and investigating the relationships between halo shapes and angular momentum.

The purely triaxial treatment of dark matter haloes overlooks another well-established result from CDM simulations: individual haloes do not have a smooth density profile – they contain sub-structure (Lacey & Cole 1993; Moore et al. 1999; Ghigna et al. 2000). While the triaxial nature of dark matter haloes can be expressed empirically (e.g. Jing & Suto 2002), quantifying the sub-structure remains a challenge. A shapelet-space representation of dark matter haloes provides a potential solution.

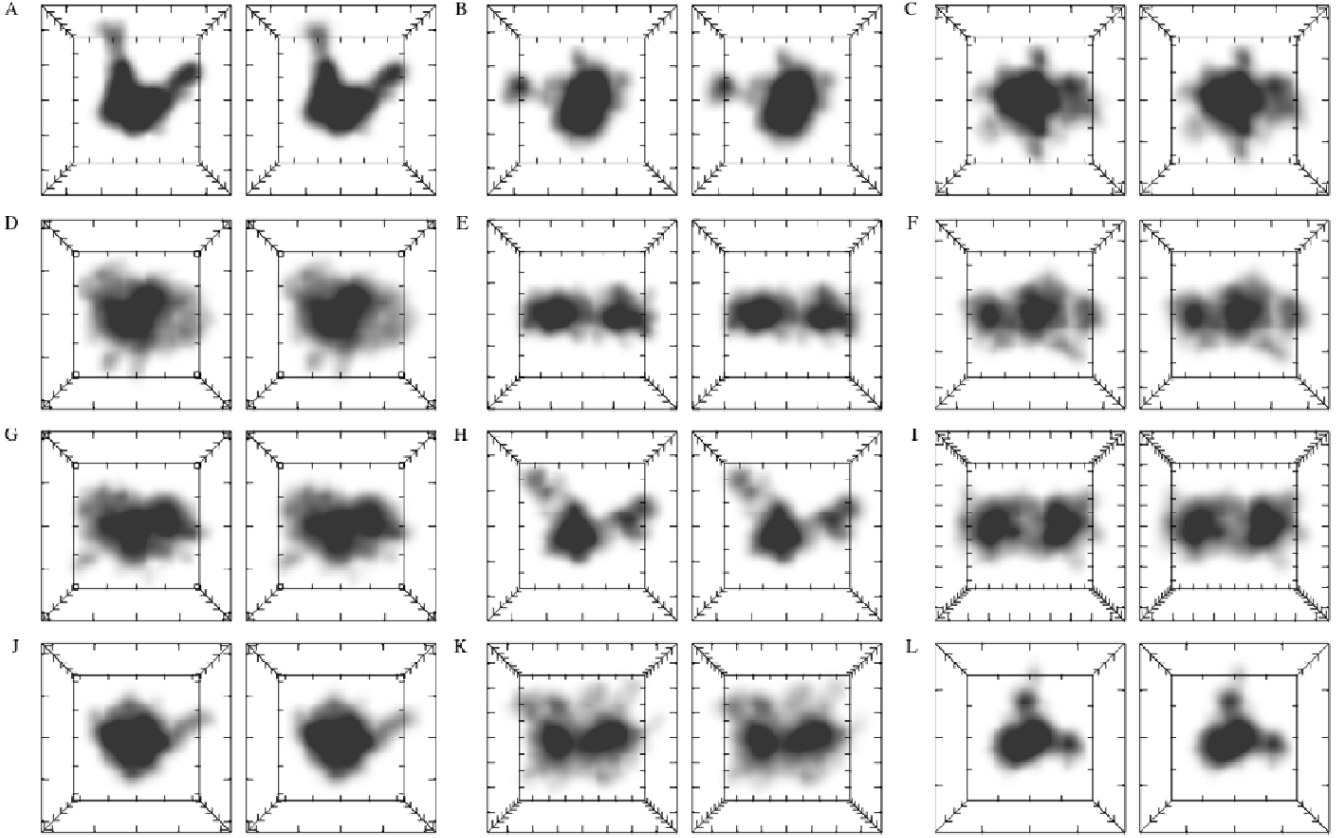


Figure 3. The 12 most massive haloes from most massive (A; top left) to least massive (L; bottom right). Each panel comprises (left) input dark matter halo and (right) shapelet reconstructed halo, displayed as volume renderings of the logarithmic density. The coordinate ranges in each panel are not equal, but have been selected for clarity based on Δx for each halo. Shapelet parameters were $N_g = 51$, $n_{\max} = 24$, and β values are in Table 1. The strong similarity between the input and shapelet reconstructed versions is apparent.

To demonstrate our approach, we use a sample of 200 candidate dark matter haloes selected from a cosmological N -body simulation performed with GADGET-2 (Springel 2005). The cosmological parameters were $\Omega_0 = 0.27$, $\Lambda_0 = 0.73$, $h = 0.71$ and $\sigma_8 = 0.9$, and candidate haloes were identified using the SubFind groupfinder (Springel et al. 2001).

Using particle number, N_p , as a proxy for mass, we pay particular attention to the twelve most massive haloes, haloes A–L, and the twelve least massive, haloes M–X, from the sample. We consider these two-subsets as being representative of typical halo shapes and presence of sub-structure, along with limiting any mass-dependent biases that may occur. For each halo, the triaxiality, T , is calculated using the approach described in Appendix B, and tabulated in Table 1. Further quantities presented in this table are described below.

Of the twelve ‘heavy’ haloes, two are oblate ($T \leq 1/3$), eight are prolate ($T \geq 2/3$) and two are triaxial ($1/3 < T < 2/3$). Both the oblate haloes (A and L) have clear central cores, while the triaxial haloes (D and J) do not possess such a core. None of the ‘light’ haloes are oblate, ten were prolate, and two were triaxial (this time, haloes with central cores).

We perform a three-dimensional shapelet decomposition on each halo, with the following input parameters fixed: $N_g = 51$, $n_{\max} = 24$ and $\beta = \beta_{\text{scale}} x_{\max} / \sqrt{2N_g}$. To select an

appropriate β_{scale} for classification of halo shapes, we define a fitness estimator in terms of the peak signal-to-noise ratio:

$$P_s = 20 \log_{10} \left[\frac{\text{Max}(f_{ijk})}{\sqrt{M_s}} \right], \quad (84)$$

where $\text{Max}(f_{ijk})$ is the maximum value in the volume, and the mean-square error is:

$$M_s = \frac{1}{N_g^3} \sum_{i,j,k=1}^{N_g} |f_{ijk} - \hat{f}_{ijk}|^2. \quad (85)$$

We calculate the average peak signal-to-noise ratio, $\langle P_s \rangle$, over 200 input haloes (Figure 2 – markers; black solid line); dashed lines represent the one-standard deviation error range. On the basis of this analysis, we choose $\beta_{\text{scale}} = 0.8$ as providing the best fit to the input halo shapes, presenting a reasonable compromise to a full optimisation process.

To avoid orientation-dependent effects, haloes are rotated such that their principle axes are aligned with the coordinate axes (see Appendix B). Halo particles are then smoothed to a grid using the triangle-shaped cloud smoothing strategy, providing number counts per voxel, which is equivalent to a density, ρ_{ijk} . To deal with the large dynamic range in ρ_{ijk} , the input shape is actually:

$$f_{ijk} = \log_{10} (1 + \rho_{ijk}). \quad (86)$$

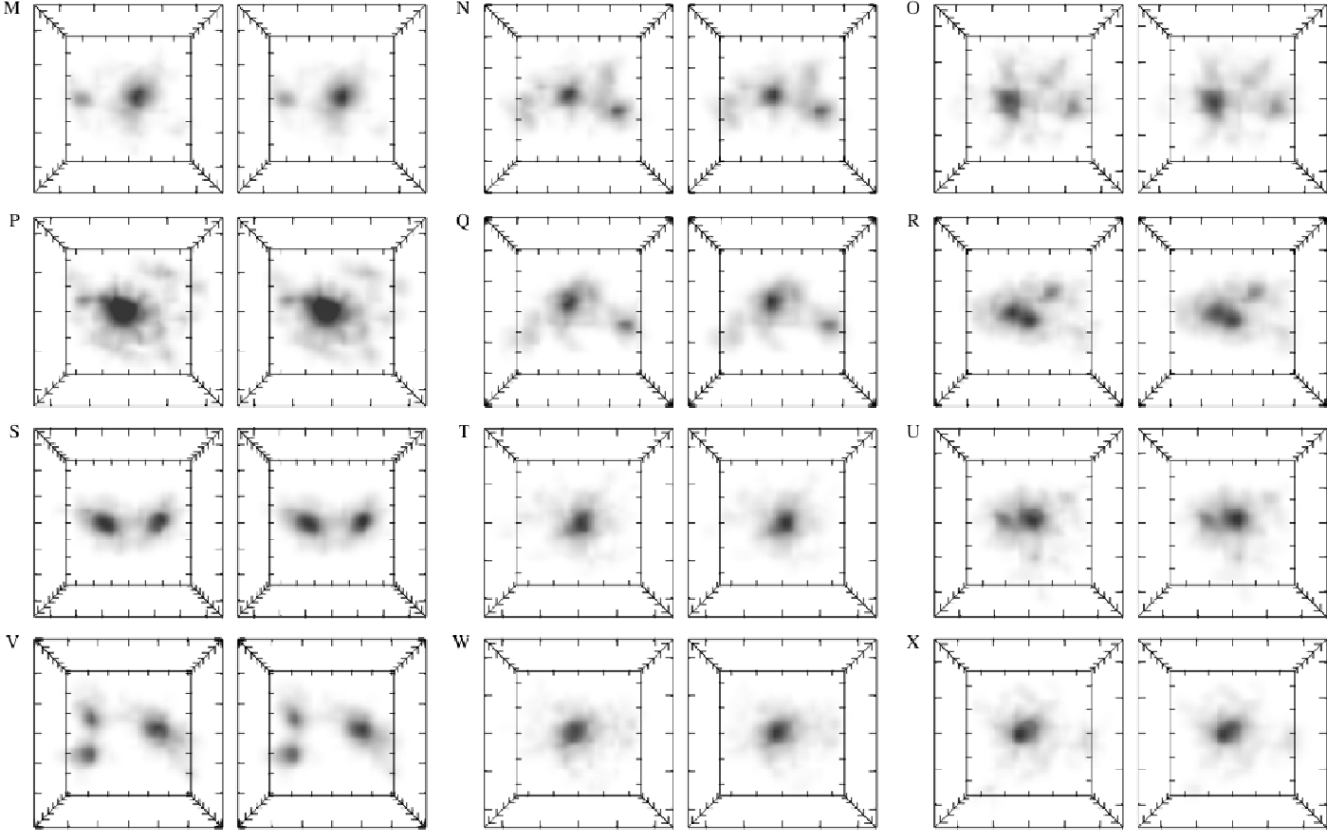


Figure 4. The 12 least massive haloes from most massive (M; top left) to least massive (X; bottom right). Each panel comprises (left) input dark matter halo and (right) shapelet reconstructed halo, displayed as volume renderings of the logarithmic density. The coordinate ranges in each panel are not equal, but have been selected for clarity based on Δx for each halo. Shapelet parameters were $N_g = 51$, $n_{\max} = 24$, and β values are in Table 1. The strong similarity between the input and shapelet reconstructed versions is apparent.

Since each halo has a different mass and hence physical extent, the β value for each halo is different – see Table 1. The other columns in this table are: the cell-width, Δx , as defined in equation (75); the maximum voxel value from the input shape, I_{\max} , and the minimum and maximum shapelet-recovered values, S_{\min} and S_{\max} , respectively. To enable quantitative comparisons between the input and reconstructed shapes we compute the quantities $\Sigma_I = \sum_{i,j,k} f_{ijk}$ and $\Sigma_S = \sum_{i,j,k} \hat{f}_{ijk}$, and P_s . Numerical testing, where reconstructions were optimised by hand, suggested that $\Sigma_I \sim \Sigma_S$ and $P_s \geq 45$ (Figure 2) represented a good shapelet fit for the grid resolution used.

The m -th most dominant shapelet component of the reconstruction has $\mathbf{n} = \mathbf{D}_m$, with amplitude $f_{3,\mathbf{D}_m} = f_{m,\max}$. Except where indicated, $\mathbf{D}_1 = (0, 0, 0)$, so we also report the value of \mathbf{D}_2 . The final two columns of Table 1 represent the result of ‘by-eye’ classifications of the spatial characteristics of each halo, $C(I)$, and the shapelet profiles, $C(S)$, into the three halo classes – see Section 5.2 below.

Figs. 3 and 4 show the results of the shapelet decomposition. For each halo, the left-hand panel shows the input shape, and the right-hand panel is reconstructed in shapelet space. Each image pair presents two-dimensional projections of fully three-dimensional, volume rendered structures. Visual comparison of pairs of images suggests that, qualitatively, Cartesian shapelets represent an appropriate basis

set for decomposition of dark matter haloes. Quantitatively, we find that:

$$|(S_{\max} - S_{\min}) / I_{\max} - 1| \leq 6\%, \quad (87)$$

$$|\Sigma_S / \Sigma_I - 1| \leq 1\%, \quad (88)$$

and $P_s \geq 45$, so that even without a halo-specific optimisation, there is excellent agreement between the input halo and its Cartesian shapelet reconstruction.

5.2 Towards an automated shape classifier

The 3-d shapelet approach provides a means to check the outcome of halo finding algorithms by identifying classes in shapelet space without needing to visually inspect entire halo-candidate catalogues. For 21 of the 24 haloes in Table 1, the dominant component is $\mathbf{D}_1 = (0, 0, 0)$ – in most cases, the zeroth-order shape has a high amplitude, which is not unexpected for haloes centred on the coordinate origin. Three haloes (I, S and V), however, receive their maximal contribution from a higher-order shapelet, $\mathbf{D}_1 = (n_1, 0, 0)$, $n_1 \geq 1$. We can use information on the relative contributions of shapelet orders higher than the zeroth order term to enable a shapelet-based classification of dark matter halo shapes.

Fig. 5 shows three characteristic patterns in shapelet

Table 1. Summary of halo properties and shapelet decomposition parameters for the sample of 24 dark matter haloes, classified into heavy (A-L) and light (M-X) samples. Table columns are: halo identifier; number of particles in halo, N_p , a proxy for halo mass; halo triaxiality, T , determined from particle positions; scale parameter, β , used for decomposition; the cell-width, Δx , as defined in equation (75); the maximum voxel values from the input shape, I_{\max} , and the shapelet-recovered minimum and maximum voxel values, S_{\min} and S_{\max} ; and $\Sigma_I = \sum_{i,j,k} f_{ijk}$ and $\Sigma_S = \sum_{i,j,k} \hat{f}_{ijk}$ are used to characterise the recovered shapes, along with the peak signal-to-noise, P_S . The m -th most dominant shapelet component has $\mathbf{n} = \mathbf{D}_m$, with amplitude $f_{3,\mathbf{D}_m} = f_{m,\max}$, and $m = 1, 2, \dots$; except where indicated, $\mathbf{D}_1 = (0, 0, 0)$, so we also present results for \mathbf{D}_2 . Halo classes are assigned ‘by eye’ through inspection of the real-space, C_I , and shapelet-space, C_S , representations – see Section 5.2 for details.

Halo	N_p	T	β	Δx	I_{\max}	Σ_I	S_{\min}	S_{\max}	Σ_S	P_S	$f_{1,\max}$	\mathbf{D}_1	\mathbf{D}_2	C_I	C_S
A	1425030	0.239	0.85	0.42	4.64	2734.9	-0.22	4.51	2739.8	47.27	15.307		(2,0,0)	2	2
B	62492	0.753	0.22	0.11	3.18	2089.5	-0.07	3.11	2093.6	51.29	1.279		(0,2,0)	2	2
C	47535	0.707	0.18	0.09	3.17	2455.0	-0.10	3.06	2457.2	50.27	0.900		(2,0,0)	2	2
D	45760	0.406	0.17	0.09	3.02	2245.5	-0.07	2.94	2245.1	51.38	0.826		(2,0,0)	2	2
E	43091	0.973	0.24	0.12	2.88	1465.3	-0.08	2.81	1465.8	49.73	0.848		(2,0,0)	3	3
F	39700	0.871	0.20	0.10	3.01	1715.0	-0.07	2.91	1715.3	51.06	0.905		(2,0,0)	2	2-3
G	37735	0.816	0.17	0.08	2.96	2132.9	-0.08	2.89	2133.5	51.01	0.753		(2,0,0)	2	2-3
H	35417	0.694	0.21	0.11	2.94	1406.5	-0.08	2.86	1406.5	51.00	0.891		(2,0,0)	2	2
I	28290	0.963	0.15	0.07	2.74	1934.3	-0.06	2.62	1933.4	49.38	0.372	(2,0,0)	(0,0,0)	3	3
J	27189	0.659	0.18	0.09	2.64	1567.1	-0.06	2.55	1568.0	51.98	0.744		(2,0,0)	2	2-3
K	21336	0.766	0.12	0.06	2.53	1863.9	-0.07	2.45	1858.4	47.46	0.313		(2,0,0)	3	3-2
L	20476	0.144	0.16	0.08	2.63	1184.9	-0.06	2.53	1185.3	54.14	0.569		(2,0,0)	2	2
<hr/>															
M	864	0.868	0.04	0.02	1.39	230.83	-0.02	1.30	229.85	52.35	0.018		(1,0,0)	2	2-1
N	855	0.934	0.05	0.02	1.24	252.54	-0.02	1.15	252.41	51.01	0.016		(2,0,0)	2	2-1
O	845	0.716	0.04	0.02	1.15	261.30	-0.02	1.07	261.67	50.01	0.011		(2,0,0)	3	3-2
P	834	0.760	0.04	0.02	0.77	271.24	-0.02	0.75	270.65	45.70	0.014		(2,0,0)	2	1
Q	829	0.818	0.05	0.02	1.21	237.36	-0.03	1.14	236.67	50.82	0.017		(0,1,0)	2	2
R	824	0.859	0.05	0.02	1.09	241.40	-0.02	1.02	240.89	50.11	0.020		(2,0,0)	3	2
S	821	0.984	0.06	0.03	1.14	212.54	-0.02	1.09	212.77	52.70	0.024	(2,0,0)	(4,0,0)	3	3
T	816	0.713	0.04	0.02	1.37	227.73	-0.02	1.27	228.45	53.16	0.018		(2,0,2)	1	1
U	797	0.422	0.04	0.02	1.14	229.69	-0.02	1.07	229.43	51.36	0.018		(2,0,0)	2	2-1
V	794	0.847	0.05	0.02	1.09	226.23	-0.03	1.02	227.14	49.75	0.013	(4,0,0)	(2,0,0)	3	3
W	788	0.876	0.04	0.02	1.32	228.40	-0.02	1.25	227.70	52.35	0.017		(1,0,0)	1	1
X	778	0.512	0.04	0.02	1.26	214.21	-0.02	1.18	213.40	51.27	0.018		(1,0,0)	1	1

space, consistent with the general appearance of the haloes in Figs. 3 and 4. For each halo, all amplitudes are plotted in index order, with n_3 value varying most rapidly, then n_2 , and finally n_1 . The light grey vertical lines indicate values of $(n_1, 0, 0)$ where $n_1 = 0, 1, \dots, n_{\max}$; for $n_{\max} = 24$, there are $N_{\text{eval}} = 2925$ shapelet coefficients. Shapelet amplitudes, represented by vertical black line segments, are plotted as $w_{\mathbf{n}} = f_{3,\mathbf{n}}/f_{1,\max}$, with the six most-dominant shapelet orders numbered and coloured red. We propose the following three classes:

- **Class 1:** Halo T (top panel) has a central core, but no significant sub-structure. In shapelet space, it is dominated by the zeroth-order shapelet, with low amplitudes for higher orders.
- **Class 2:** Halo D (middle panel) has a central core, and obvious sub-structure. Here, the zeroth-order shapelet again dominates, but there are several higher order shapelets with amplitudes $\lesssim \frac{1}{2}f_{1,\max}$.
- **Class 3:** Halo I (bottom panel) has significant sub-structure and no central core. The zeroth shapelet is no longer always the dominant term, and there are several shapelet orders with amplitudes $\sim f_{1,\max}$.

The initial alignment of each halo with the x -axis is apparent, with obvious contributions from shapelet orders $\mathbf{n} = (n_1, 0, 0)$.

The flexibility of the classification system is demon-

strated in Figs. 6-8. We select three new intermediate mass haloes: Haloes 100, 101 and 102 (specific properties are listed in the captions). Performing shapelet decomposition on these haloes with arbitrary three-dimensional rotations, thus removing the alignment of the principle moments of inertia with the coordinate axes, we see that the basic features of the three shapelet classes remain. Haloes 100 and 101, with $f_{1,\max}$ occurring for the zeroth-order shapelet, retain this behaviour, while the power in higher shapelet orders is distributed away from the $(n_1, 0, 0)$ values. This is not unexpected from the behaviour of 2-d shapelets under rotations (see Refregier 2003). Rotation of Halo 102 (Fig. 8), with two clear components, results in variation in the highest-amplitude shapelet coefficients, suggesting the following features for identification of haloes of this type: either $f_{1,\max}$ occurs for a shapelet order other than the zeroth-order, or there are one or more shapelet orders with amplitudes $\gtrsim 0.5f_{1,\max}$.

We use this heuristic to now attempt a purely (by-eye) shapelet-based selection of haloes with clear multiple sub-structures (Class 3). We apply the shapelet decomposition with the same input parameters as used throughout this initial implementation, to a total of 176 haloes. Particle counts for this new set of haloes are in the range $865 \leq N_p \leq 20033$, noting that these haloes are at intermediate masses to the 24 investigated previously. We identify 44 Class 3 haloes on the basis of their shapelet representation, the first 36 of which are shown in Fig. 9, and all of which exhibit the

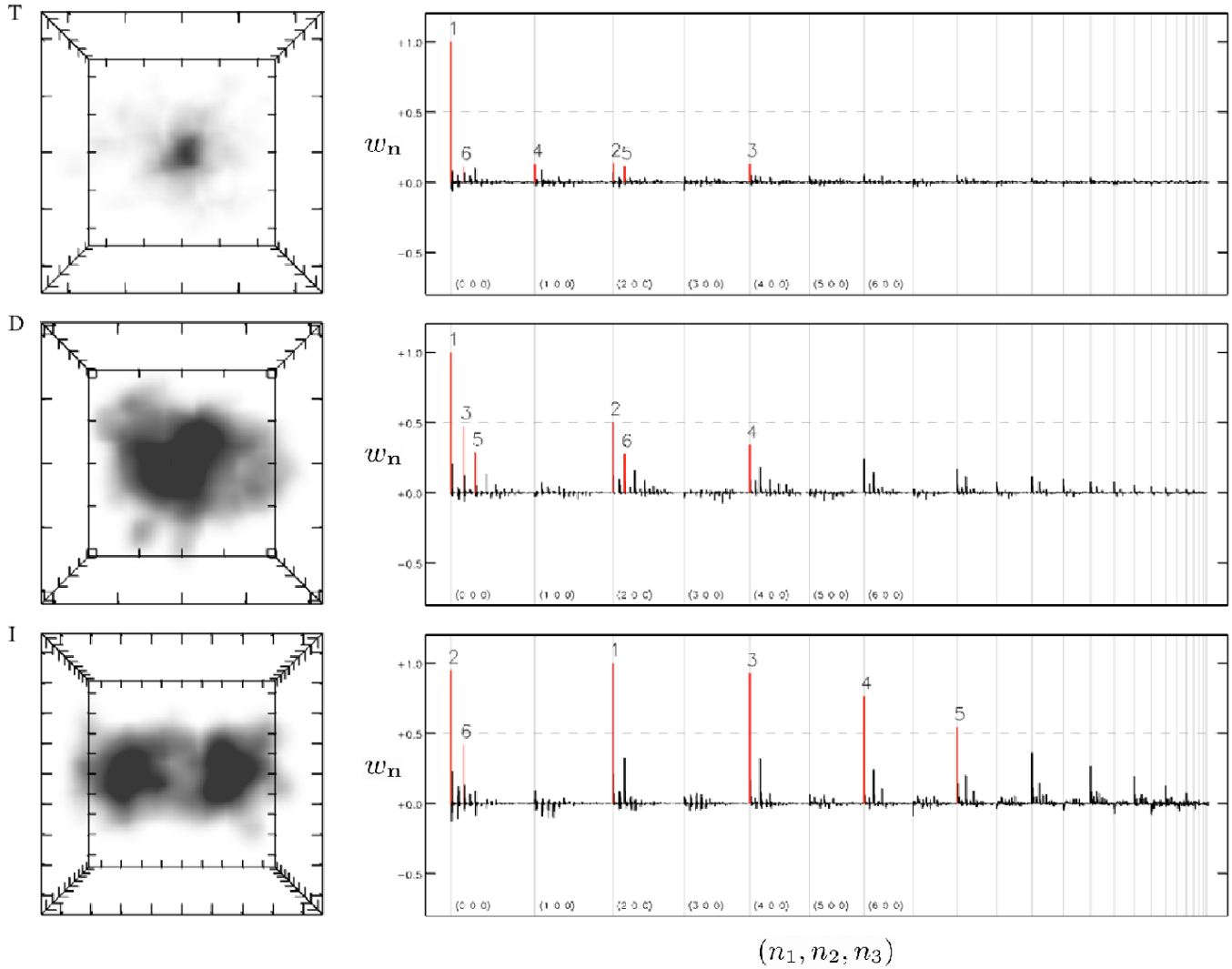


Figure 5. Three characteristic shapelet-space representations of dark matter haloes. Shapelet coefficient amplitudes are plotted in index order, with n_3 value varying most rapidly, then n_2 , and finally n_1 – the light grey vertical lines indicate values of $(n_1, 0, 0)$ with $n_1 = 0, 1, \dots, n_{\max}$. Shapelet amplitudes, represented by vertical black line segments, are $w_{3,\mathbf{n}} = f_{3,\mathbf{n}}/f_{1,\max}$, with the six most dominant shapelet orders numbered and coloured red. (Top) Halo T, Class 1 – central core, no significant sub-structure – dominated by zeroth-order shapelet, low-amplitude for higher orders. (Middle) Halo D, Class 2 – central core, significant sub-structure – f_{\max} occurs at $\mathbf{n} = (0, 0, 0)$ and several higher order shapelets have amplitudes $\sim \frac{1}{2}f_{\max}$. Bottom) Halo I, Class 3 – significant sub-structure, no central core – zeroth-order shapelet is not the dominant term (although in other Class 3 haloes, it can still be dominant), several orders with amplitudes $\sim f_{\max}$.

expected spatial characteristics. Visual inspection of the remaining 132 haloes suggests a further 10 haloes that should have been identified from their shapelet representations. In all cases, reinvestigation of the shapelet distribution revealed that they were very close to meeting the criteria for a Class 3-halo. While a more robust approach to classification is required for a full implementation (e.g. using an appropriately-sized training set and the construction of a decision tree or neural network classifier), our results do suggest that there is benefit to performing classification of dark matter halo shapes in shapelet space.

The existence of multiple cores in the dark matter haloes has implications for computation of halo triaxiality – the classification of ‘heavy’ haloes E, F, I, K as prolate based

purely on the principle moments of inertia is somewhat misleading; in each case, an argument could be made that an isolated group has not been identified using, in this case, the Subfind algorithm. Our application to 176 haloes identifies 44(+10) prolate haloes where the inferred triaxiality was based on counting potentially distinguishable sub-haloes as a single halo. A shapelet-based automated classifier provides a method of identifying such haloes without needing to visually inspect each halo.

5.3 Shapelet-based quantification

As an example of quantitative analysis in shapelet space, we calculate the moment of inertia tensors from equation

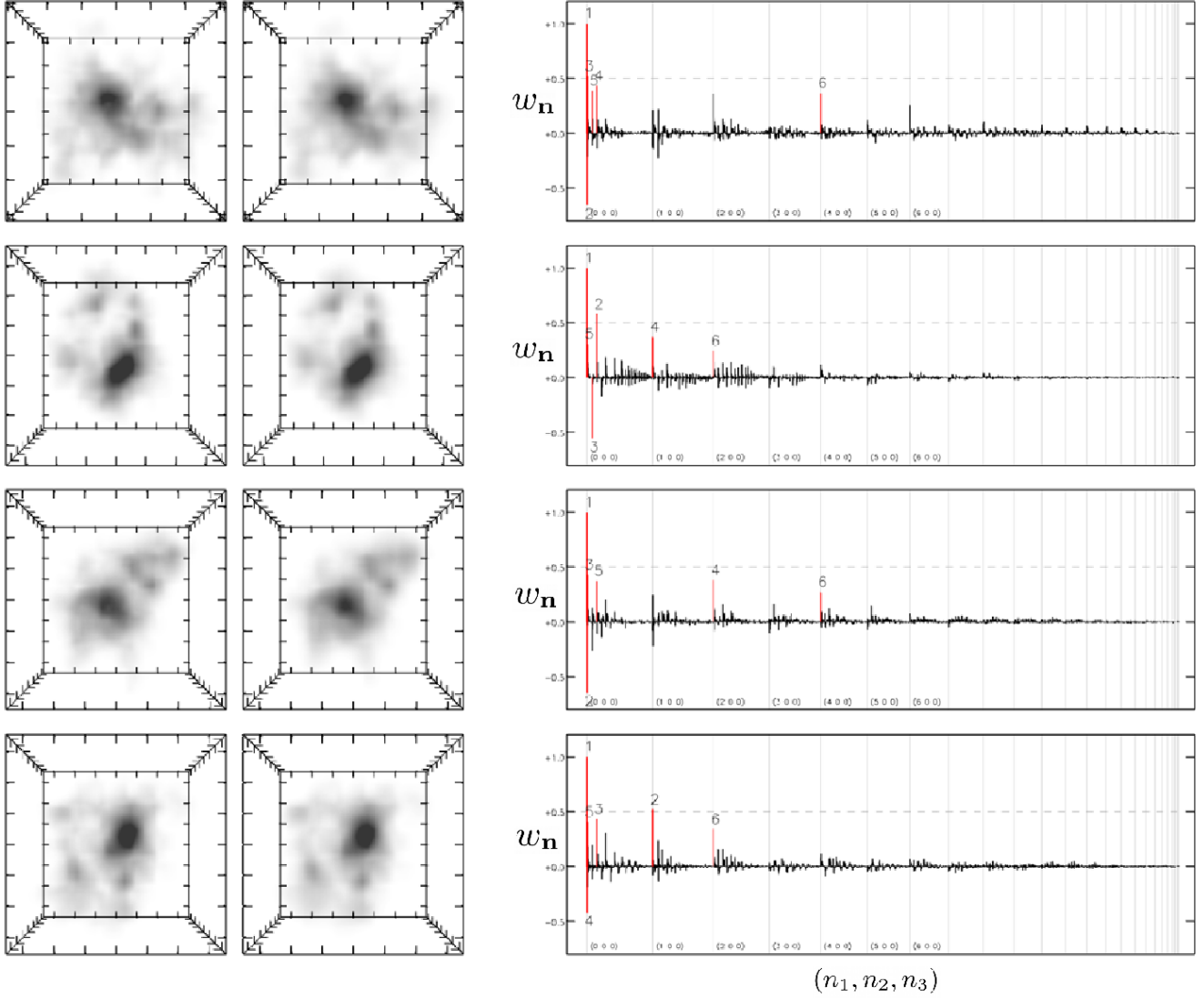


Figure 6. Halo 100, $N_p = 2068$, $T = 0.80$ (prolate), Class 2. The left-hand column shows four real-space configurations of the halo, with arbitrary rotations about the centre-of-mass. The right-hand column shows the corresponding shapelet-space configuration; $w_{\mathbf{n}} = f_{3,\mathbf{n}}/f_{1,\max}$, and the horizontal axis represents the sequential coefficients, \mathbf{n} – see Section 5.2. General properties of the distribution of shapelet amplitudes are preserved regardless of orientation.

(43)–(45) and hence triaxiality, T . In Fig. 10, we plot the shapelet-based triaxiality, T_S , against the value determined from the original particle positions, T , for the sample of 176 intermediate mass haloes. A least-squares fit to the data (solid line) gives $T_S = 0.96T + 0.02$ with the Pearson coefficient, $r = 0.98$. In Fig. 11, we plot the ratio of T_S/T against the particle number, N_p , which suggests that there is a slightly larger scatter for the lower mass haloes. We find that $\langle T_S/T \rangle = 0.99 \pm 0.12$, where the error is the sample standard deviation. Even though we have not performed a per-halo optimisation for $(\beta, n_{\max}, \mathbf{x}_c)$, the shapelet-based analytic result does indeed provide a very good estimator for the halo triaxiality.

6 SUMMARY AND OUTLOOK

We have extended the two-dimensional Cartesian shapelet formalism of Refregier (2003) to three dimensions, deriving analytic expressions for the zeroth moment, object centroid, root-mean-square radius, and the components of the quadrupole moment and moment of inertia tensors. We also presented generalisations to d -dimensions.

Further work is necessary to develop a robust and systematic optimisation strategy for the decomposition parameters, and the development of specific applications for the three-dimensional shapelet technique requires such a strategy. There are also opportunities to develop the formalism further, specifically extending it to include spherical shapelet functions [c.f. the alternative presentation of

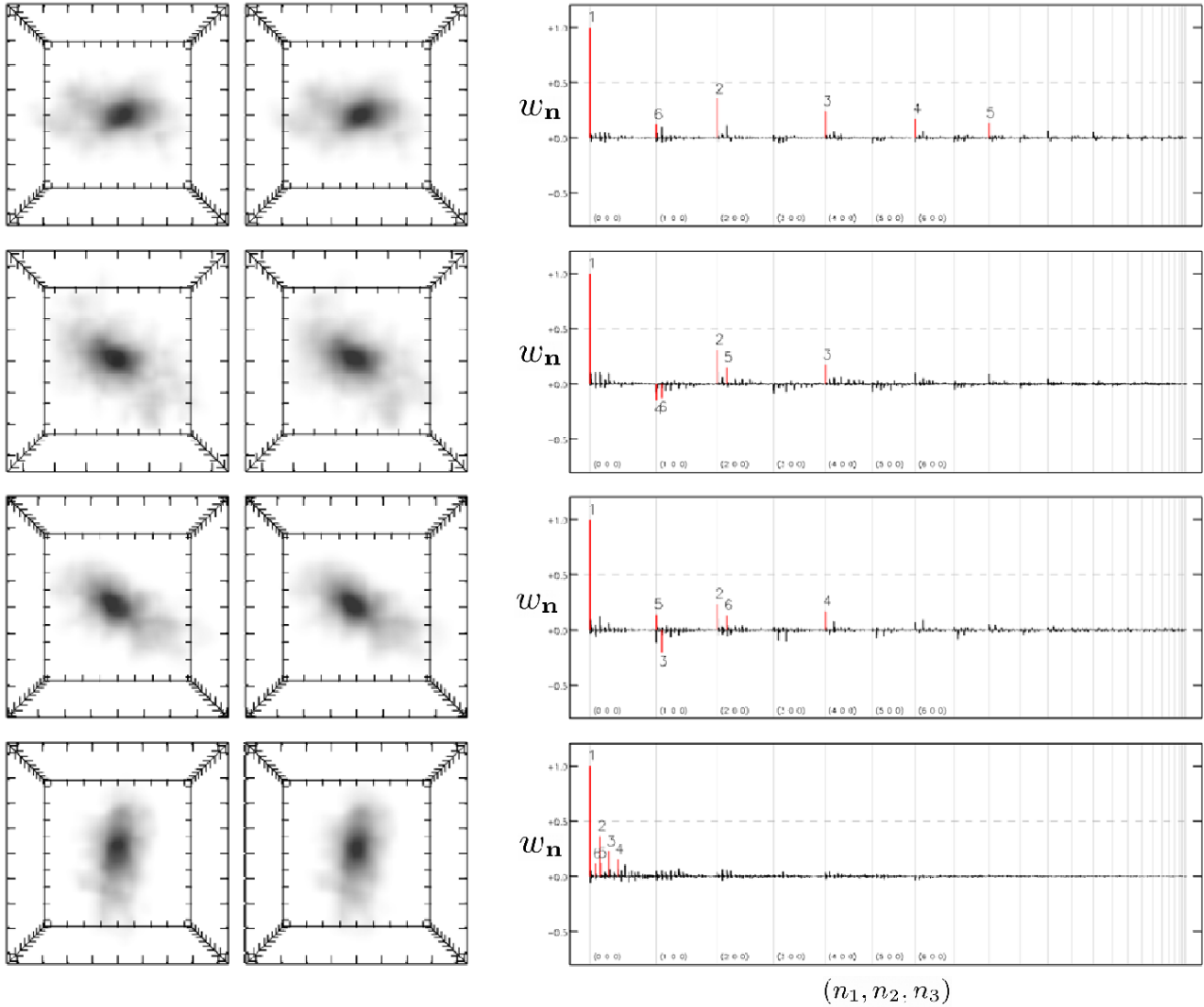


Figure 7. Halo 101, $N_p = 2047$, $T = 0.92$ (prolate), Class 1. The left-hand column shows four real-space configurations of the halo, with arbitrary rotations about the centre-of-mass. The right-hand column shows the corresponding shapelet-space configuration; $w_n = f_{3,n}/f_{1,\max}$, and the horizontal axis represents the sequential coefficients, \mathbf{n} – see Section 5.2. General properties of the distribution of shapelet amplitudes are preserved regardless of orientation.

two-dimensional Cartesian shapelets as polar shapelets by Massey & Refregier (2005)].

The shapelet decomposition algorithm exhibits attributes that make it an ideal target for implementation on modern, massively-parallel GPUs. Our algorithm analysis demonstrates that the computation is entirely (or embarrassingly) parallel; has minimal or no branching; maintains a high ratio of arithmetic operations to memory-access operations; and has a memory access pattern that will result in aligned or contiguous access to memory, required for achieving a high memory throughput. With our proposed scheme of precomputing shapelet voxel-integral terms, the computation reduces to a parallel series of multiply-add operations, which are almost ideal for GPUs – we anticipate achieving close to peak processing performance. Significantly reducing the computation time for the shapelet decomposition,

compared to CPU, means that more processing time is then available for optimisation.

As an example application, we have demonstrated how three-dimensional shapelets can be used to study the complex sub-structures of dark matter haloes from cosmological N -body simulations, including providing an alternative approach to classifying the properties of haloes. Our preliminary investigation suggests that halo triaxiality measured purely from the moment of inertia tensor may be incorrect due to limitations of group finders that are not able to separate out what may be truly distinct sub-clumps. Improvements to our current ‘by eye’ approach to classification could include development of a decision tree or neural network classifier, or the use of principle component analysis to significantly reduce the number of shapelet terms required for classification (Kelly & McKay 2004).

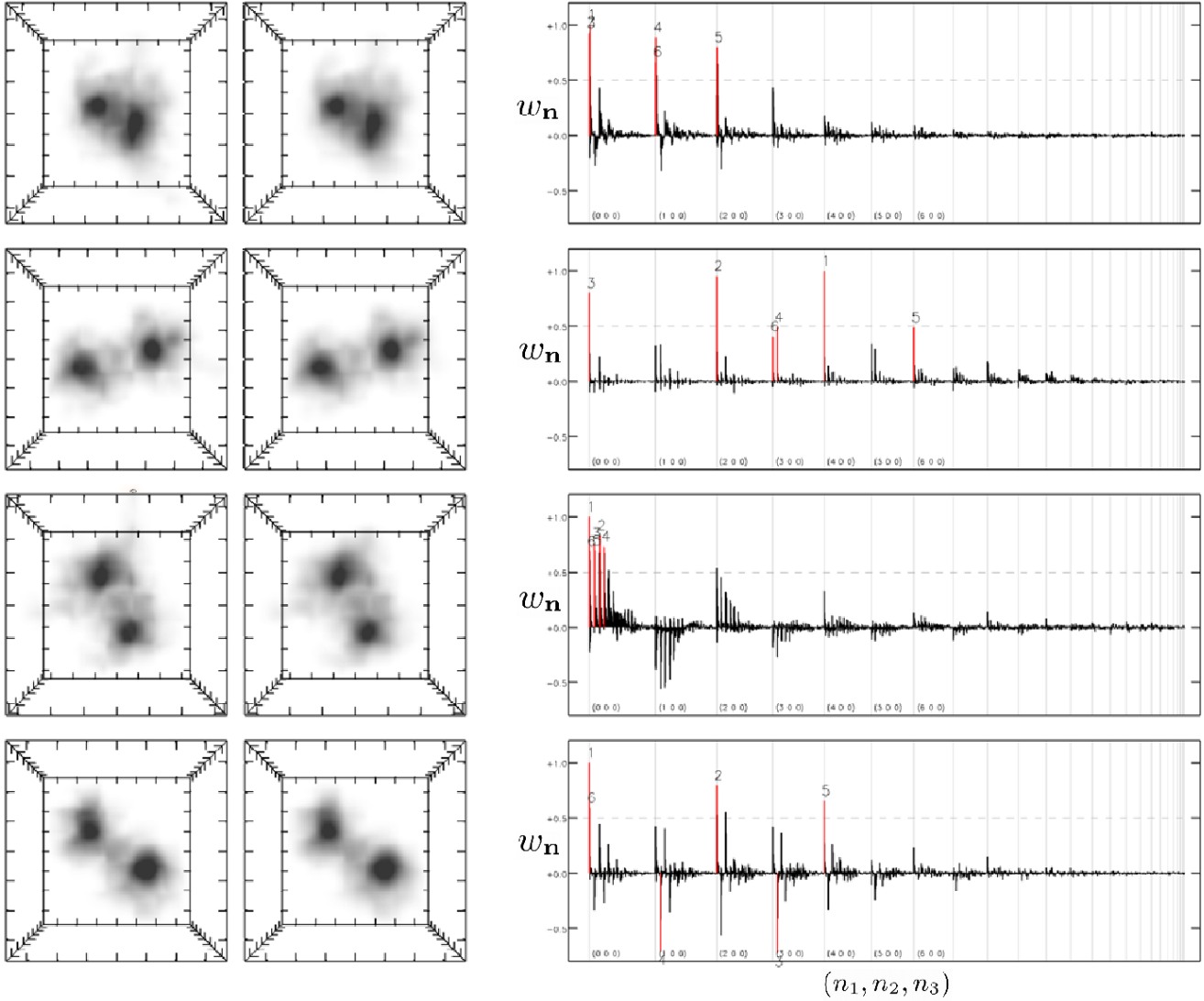


Figure 8. Halo 102, $N_p = 2005$, $T = 0.91$ (prolate), Class 3. The left-hand column shows four real-space configurations of the halo, with arbitrary rotations about the centre-of-mass; the right-hand column shows the corresponding shapelet-space configuration; $w_{\mathbf{n}} = f_{3,\mathbf{n}}/f_{1,\max}$, and the horizontal axis represents the sequential coefficients, \mathbf{n} – see Section 5.2. General properties of the distribution of shapelet amplitudes are preserved regardless of orientation.

The shapelet formalism is virtually unexplored in the three-dimensional domain, offering opportunities for the further development of a methodology that can be used to quantify and analyse complex three-dimensional structures. Future applications of the three-dimensional shapelet technique may include classification and parameterisation of sources identified in HI spectral line data cubes; studying the shapes of voids in cosmological simulations (by considering an inverted density field); and the possibility to generate mock dark matter haloes through an extensive study of the distribution of shapelet amplitudes as a function of mass and triaxiality.

ACKNOWLEDGMENTS

This research was supported under the Australian Research Council’s Discovery Projects funding scheme (project number DP0665574). PL is supported by the Alexander von Humboldt Foundation. CJF is grateful to Michael Vanner and Toffa Beer for their contributions to this work. We thank Chris Power for providing the dark matter halo sample, David Bacon for early discussions on shapelets, and our referee for his insightful comments. Three-dimensional visualisation was conducted with the S2PLOT programming library (Barnes et al. 2006).

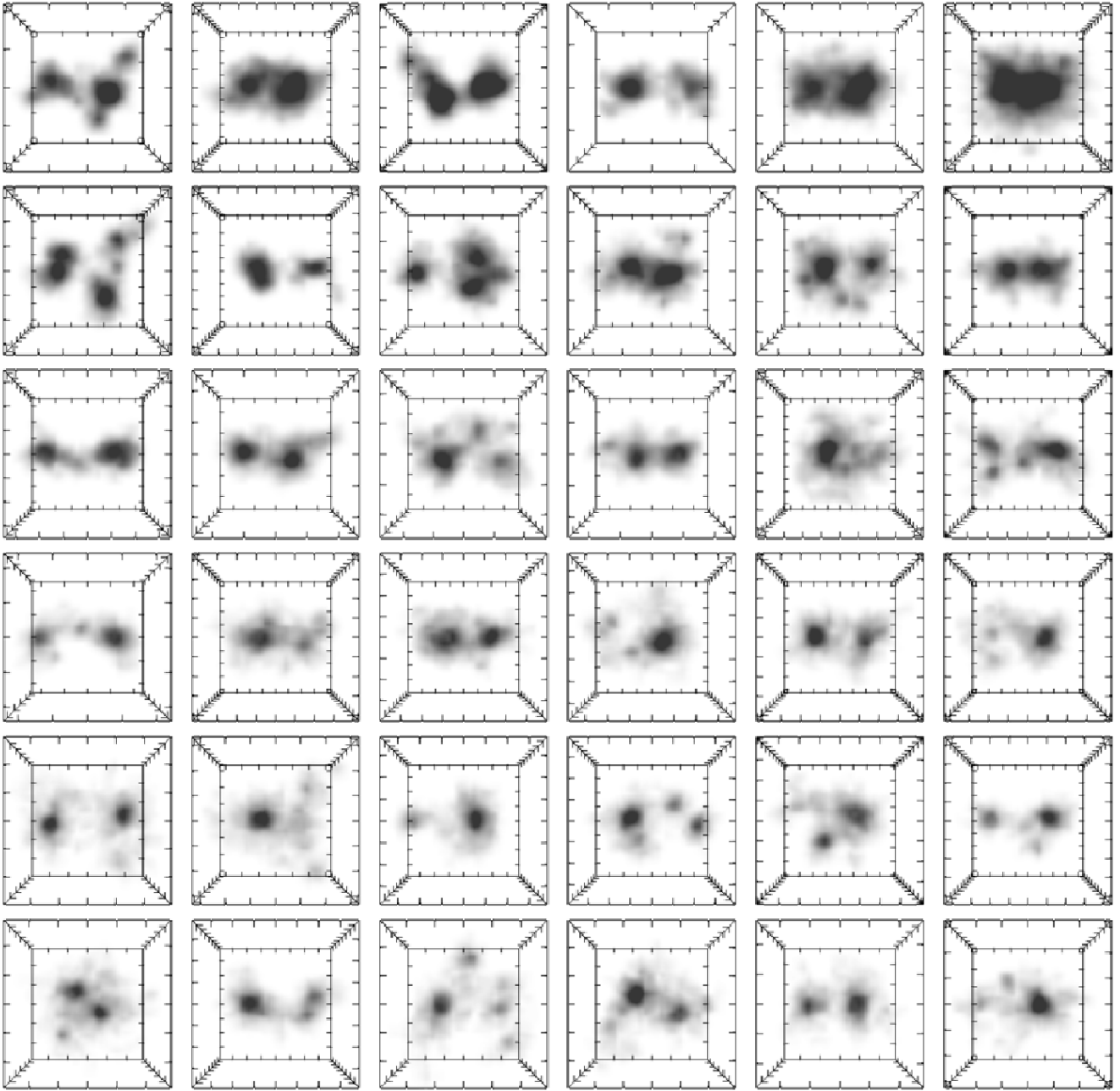


Figure 9. From a visual investigation of 176 haloes in shapelet coefficient space, 44 were selected as having obvious sub-structure and no central core. 36 of these haloes are shown here. Visual inspection of the remaining 130 haloes in real space suggests that an additional 10 should have been identified as Class 3. Further inspection in shapelet space confirmed the limitation of a ‘by-eye’ classifier.

REFERENCES

- Allgood B., Flores R.A., Primack J.R., Kravtsov A.V., Wechsler R.H., Faltenbacher A., Bullock J.S., 2006, *MNRAS*, 367, 1781
- Andrae, R., Jahnke, K., Melchior, P., 2011, *MNRAS*, 411, 385
- Bailin J., Steinmatz M., 2005, *ApJ*, 627, 647
- Barrow J.D., Bhavsar S.P., Sonoda D.H. 1985, *MNRAS*, 216, 17
- Barnes D.G., Fluke C.J., Bourke P.D., Parry O.T., 2006, *PASA*, 23, 82
- Barnes, J., Efstathiou, G., 1987, *ApJ*, 319, 575
- Barsdell, B.R., Barnes D.G., Fluke C.J., 2010, *MNRAS*, 408, 1936
- Berry R.H., Hobson M.P., Withington S., 2004, *MNRAS*, 354, 199
- Bosch, J., 2010, *AJ*, 140, 870
- Chang T.-C., Refregier A., Helfand D.J., 2004, *ApJ*, 617, 794
- Coffey M.W., 2006, *JPhys A: Math Gen*, 39, 877
- Cole S., Lacey C., 1996, *MNRAS*, 281, 716
- Davis, M., Efstathiou, G., Frenk, C.S., White, S.D.M.,

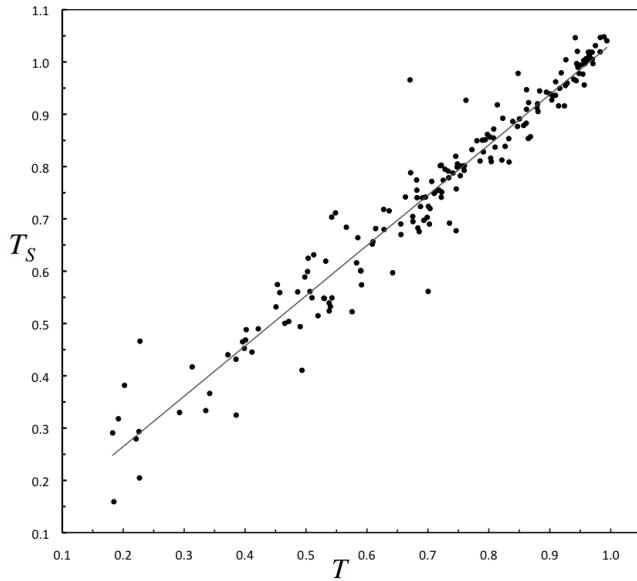


Figure 10. The shapelet-based triaxiality, T_S , plotted against the value determined from the original particle positions, T , for the sample of 176 intermediate mass haloes. A least-squares fit to the data (solid line) gives $T_S = 0.96T + 0.02$ with the Pearson coefficient, $r = 0.98$.

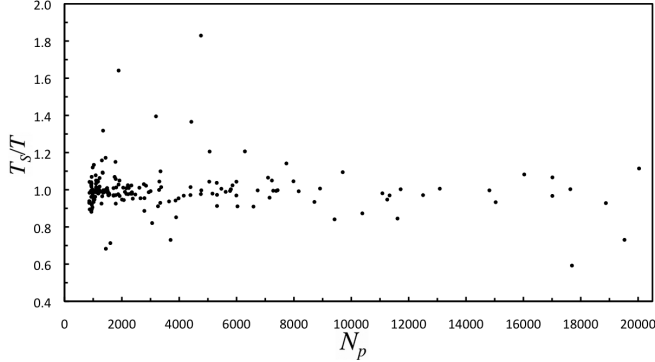


Figure 11. The ratio of the shapelet-based triaxiality to the particle-based value, T_S/T , plotted against the number of particles, N_p , in each of 176 intermediate mass haloes. We find that $\langle T_S/T \rangle = 0.99 \pm 0.12$, where the error is the sample standard deviation.

1985, ApJ, 292, 371
 Dubinski, J., 1994, ApJ, 431, 617
 Dubinski J., Carlberg R.G., 1991, ApJ, 378, 496
 Ferry M., Rhodes J., Massey R., White M., Coe D., Mobasher B., 2008, AP, 30, 65
 Franx, M., Illingworth, G., de Zeeuw, T., 1991, ApJ, 383, 112
 Frenk C.S., White S.D.M., Davis M., Efstathiou G., 1988, ApJ, 327, 507
 Ghigna S., Moore B., Governato F., Lake G., Quinn T., Stadel J., 2000, ApJ, 544, 616
 Goldberg D.M., Bacon D.J., 2005, ApJ, 619, 741
 Goodman A.A., Rosolowsky E.W., Borkin M.A., Foster J.B., Halle M., Kauffmann J., Pineda J.E., 2009, Nat, 457,

63

Gott J.R. III, Dickinson M., Melott A.L., 1986, ApJ, 306, 341
 Icke V., van de Weygaert R., 1987, A&A, 184, 16
 Jing Y.P., Suto Y., 2002, ApJ, 574, 538
 Kasun S.F., Evrard A.E., 2005, ApJ, 629, 781
 Kelly B.C., McKay T.A., 2004, AJ, 127, 625
 Knebe A., Wießner V., 2006, PASA, 23, 125
 Kuhlen, M., Diemand, J., Madau, P., 2007, ApJ, 671, 1135
 Kuijken K., A&A, 456, 827
 Lacey C., Cole S., 1993, MNRAS, 262, 627
 Massey R., Refregier A., Conselice C.J., Bacon D.J., 2004, MNRAS, 348, 214
 Massey R., Refregier A., 2005, MNRAS, 363, 197
 Massey R., Rowe B., Refregier A., Bacon D.J., Bergé J., 2007, MNRAS, 380, 229
 Mecke K.R., Buchert T., Wagner H., 1994, A&A, 288, 697
 Melchior P., Meneghetti M., Bartelmann M., 2007, A&A, 463, 1215
 Melchior P., Andrae R., Maturi M., Bartelmann M., 2009, A&A, 493, 727
 Melchior, P., Böhnert, A., Lombardi, M., Bartelmann, M., 2010, A&A, 510, A75
 Moore B., Ghigna S., Governato F., Lake G., Quinn T., Stadel J., Tozzi P., 1999, ApJ, 524, 19
 Ngan W.-H., W., van Waerbake L., Mahdavi A., Heymans C., Hoekstra H., 2009, MNRAS, 396, 1211
 Oguri M., Takada M., Umetsu K., Broadhurst T., 2005, ApJ, 632, 841
 Ossenkopf V. 1993, A&A, 280, 617
 Paulin-Henriksson S., Refregier A., Amara A., 2009, A&A, 500, 647
 Pearson R.C., Coles P., 1995, MNRAS, 272, 231
 Refregier A., 2003, MNRAS, 338, 35
 Refregier A., Bacon D., 2003, MNRAS, 338, 48
 Sahni V., Sathyaprakash B.S., Shandarin S.F., 1998, ApJ, 495, L5
 Sousbie T., Pichon C., Colombi S., Novikov D., Pogosyan D., 2008, MNRAS, 383, 1655
 Springel, V., White, S.D.M., Tormen, G., Kauffmann, G., 2001, MNRAS, 328, 726
 Springel, V., 2005, MNRAS, 364, 1105
 Stepnik B., et al., 2003, A&A, 398, 551
 White S.D.M., Frenk C.S., Davis M., Efstathiou G., 1987, ApJ, 313, 505
 Young C., Gallagher P.T., Ireland J., McAteer R., 2005, American Geophysical Union, abstract #SP11A-07

APPENDIX A: HERMITE POLYNOMIALS

We collect here a number of key expressions relating to Hermite polynomials, which prove useful in deriving the analytic properties of Section 3.

Expressing the Hermite polynomials via the Rodrigues formula

$$H_n(x) = (-1)^n e^{x^2} \frac{d^n}{dx^n} (e^{-x^2}), \quad (\text{A1})$$

one can show the important recursion relation

$$H_{n+1}(x) = 2xH_n(x) - \frac{dH_n(x)}{dx}, \quad (\text{A2})$$

which further implies the shapelet basis functions satisfy:

$$\sqrt{2(n+1)\beta}B_{n+1}(x;\beta) = \left(x - \beta^2 \frac{d}{dx}\right) B_n(x;\beta) \quad (\text{A3})$$

and

$$\left(x^2 - \beta^4 \frac{d^2}{dx^2}\right) B_n(x;\beta) = (2n+1)\beta^2 B_n(x;\beta), \quad (\text{A4})$$

which is the eigenvalue equation. Calculating the derivative terms, we have the further recurrence relations:

$$H_{n+1}(x) = 2xH_n(x) - 2nH_{n-1}(x). \quad (\text{A5})$$

APPENDIX B: TRIAXIALITY AND HALO ROTATIONS

Triaxiality of a dark matter halo is most easily expressed in terms of the principle moments of inertia. The principle moments, (I_1, I_2, I_3) , and the associated principle axes, $(\mathbf{e}_1, \mathbf{e}_2, \mathbf{e}_3)$, are the eigenvalues and eigenvectors of the moment of inertia tensor, \hat{I} , respectively. Approximating an arbitrary halo as a triaxial ellipsoid of the form

$$\frac{x^2}{a^2} + \frac{y^2}{b^2} + \frac{z^2}{c^2} = 1 \quad (\text{B1})$$

with $c \leq b \leq a$, then

$$I_1 = \frac{M}{5}(b^2 + c^2) \quad (\text{B2})$$

$$I_2 = \frac{M}{5}(a^2 + c^2) \quad (\text{B3})$$

$$I_3 = \frac{M}{5}(a^2 + b^2) \quad (\text{B4})$$

and $I_1 \leq I_2 \leq I_3$. Moreover, we can calculate the triaxiality parameter (Franx, Illingworth & de Zeeuw 1991):

$$T = \frac{a^2 - b^2}{a^2 - c^2} = \frac{I_2 - I_1}{I_3 - I_1}, \quad (\text{B5})$$

enabling us to classify haloes as oblate ($T \leq 1/3$), triaxial ($1/3 < T < 2/3$), or prolate ($T \geq 2/3$). We define a sphere ($a = b = c$) to have $T \equiv 0$.

Since we have full information on particle positions, (x, y, z) , from the cosmological simulation, we make use of this to simplify the computation of \hat{I} . Specifically, we compute elements of \hat{I} from particle positions, using standard eigensystem routines from the GNU Scientific Library⁵ to solve for the principle eigenvectors and eigenvalues. To enable comparisons between halos, we rotate each halo so that its principle axes are aligned with the Cartesian axes. First, we define an orthogonal coordinate system with unit vector directions $\mathbf{e}_1, \mathbf{e}_2$ and

$$\mathbf{n} = \mathbf{e}_1 \otimes \mathbf{e}_2. \quad (\text{B6})$$

Although \mathbf{e}_3 is orthogonal to \mathbf{e}_1 and \mathbf{e}_2 , explicitly calculating the cross-product ensures that we have a right-handed coordinate system. The Euler angles are:

$$\theta_1 = \sin^{-1}(-\mathbf{e}_{2,z}) \quad (\text{B7})$$

$$\theta_2 = \tan^{-1}(\mathbf{e}_{1,z}/\mathbf{n}_z) \quad (\text{B8})$$

$$\theta_3 = \tan^{-1}(\mathbf{e}_{2,x}/\mathbf{2}_y). \quad (\text{B9})$$

We use the standard C-function `atan2`, which returns the principle value $\tan^{-1}(y/x)$, for calculating θ_2 and θ_3 , and is recommended for converting between rectangular and polar coordinates.

Next, we build a general 3×3 rotation matrix:

$$\mathbf{R} = \begin{pmatrix} C_y C_z + S_x S_y S_z & C_x S_z & -S_y C_z + S_x C_y S_z \\ -C_y S_z + S_x S_y C_z & C_x C_z & S_y S_z + S_x C_y C_z \\ C_x S_y & -S_x & C_x C_y \end{pmatrix}, \quad (\text{B10})$$

where $C_x = \cos(\theta_x)$, $S_x = \sin(\theta_x)$ and similarly for y and z , from which we can determine the inverse matrix, \mathbf{R}^{-1} , most easily via the transpose, \mathbf{R}^T , and the adjunct matrix of \mathbf{R}^T . Each particle position, \mathbf{p} , in the halo is now rotated around the origin to new coordinates:

$$\mathbf{p}' = \mathbf{R}^{-1}\mathbf{p}. \quad (\text{B11})$$

⁵ http://www.gnu.org/software/gsl/manual/html_node/Eigensystems.html